The Astrophysical Journal, 728:48 (18pp), 2011 February 10 doi:10.1088/0004-637X/728/1/48
© 2011. The American Astronomical Society. All rights reserved. Printed in the U.S.A.

THE MASS–RADIUS(–ROTATION?) RELATION FOR LOW-MASS STARS

Adam L. Kraus[1,7], Roy A. Tucker[2], Michael I. Thompson[3], Eric R. Craine[3,4,5], and Lynne A. Hillenbrand[6]
[1] University of Hawaii-IfA, 2680 Woodlawn Dr., Honolulu, HI 96822; alk@ifa.hawaii.edu
[2] Goodricke-Pigott Observatory, 5500 West Nebraska Street, Tucson, AZ 85757, USA
[3] Global Network of Astronomical Telescopes, Inc., Tucson, AZ, USA
[4] Western Research Company, Inc., 3275 W. Ina Rd., Suite 217, Tucson, AZ 85741, USA
[5] Department of Physics, Colorado State University, Fort Collins, CO, USA
[6] Department of Astronomy MC 249-17, California Institute of Technology, 1200 E. California Blvd., Pasadena, CA 91125, USA
Received 2010 August 13; accepted 2010 November 5; published 2011 January 19

ABSTRACT

The fundamental properties of low-mass stars are not as well understood as those of their more massive counterparts. The best method for constraining these properties, especially masses and radii, is to study eclipsing binary systems, but only a small number of late-type ($\geqslant$M0) systems have been identified and well characterized to date. We present the discovery and characterization of six new M dwarf eclipsing binary systems. The 12 stars in these eclipsing systems have masses spanning 0.38–0.59 $M_{\odot}$ and orbital periods of 0.6–1.7 days, with typical uncertainties of $\sim$0.3% in mass and $\sim$0.5%–2.0% in radius. Combined with six known systems with high-precision measurements, our results reveal an intriguing trend in the low-mass regime. For stars with $M = 0.35$–$0.80\,M_{\odot}$, components in short-period binary systems ($P \lesssim 1$ day; 12 stars) have radii which are inflated by up to 10% ($\mu = 4.8\% \pm 1.0\%$) with respect to evolutionary models for low-mass main-sequence stars, whereas components in longer-period systems (>1.5 days; 12 stars) tend to have smaller radii ($\mu = 1.7\% \pm 0.7\%$). This trend supports the hypothesis that short-period systems are inflated by the influence of the close companion, most likely because they are tidally locked into very high rotation speeds that enhance activity and inhibit convection. In summary, very close binary systems are not representative of typical M dwarfs, but our results for longer-period systems indicate that the evolutionary models are broadly valid in the $M \sim 0.35$–$0.80\,M_{\odot}$ regime.

Key words: binaries: eclipsing – stars: fundamental parameters – stars: late-type – stars: low-mass – stars: rotation

Online-only material: machine-readable table, color figures

1. INTRODUCTION

M dwarfs are ubiquitous in the solar neighborhood and constitute the majority of the stellar content in our galaxy, but their fundamental properties are not as well understood as those of their more massive brethren. These measurements are crucial for calibrating stellar evolutionary models, inferring accurate masses and radii for transiting exoplanets, and understanding the evolution of low-mass companions in compact binaries. These properties (mass, radius, luminosity and effective temperature) are typically calibrated by observations of binary systems. However, since M dwarfs are intrinsically faint, a very limited sample of M dwarf eclipsing binaries (MDEBs) is accessible and suitable for a more detailed study. The radii of low-mass stars have been particularly difficult to study since they can be measured with high precision ($\sigma \lesssim$ 1%–2%) only in double-lined eclipsing binary (EB) systems, which must be identified in wide-field, multi-epoch variability studies. To date, only $\sim$10 systems with primary masses $\lesssim 0.6\,M_{\odot}$ have been identified, and only a handful of those have been characterized with the necessary precision.

Preliminary results for the few well-studied systems have found a troubling level of disagreement with theoretical models. Most of the components in low-mass eclipsing systems appear to be 5%–15% larger than theoretical models would predict (e.g., Lacy 1977; Leung & Scheider 1978; López-Morales & Ribas 2005; Bayless & Orosz 2006; Irwin et al. 2009), and this excess is seen for a wide range of stellar masses (0.2–0.8 $M_{\odot}$). However, it is unclear whether the larger radii indicate a general problem in models (i.e., due to missing opacities) or a systematic effect specific to eclipsing systems. For example, most close binary systems are tidally locked into very rapid rotation, which could lead to stronger magnetic fields than for slow-rotating single stars (e.g., Chabrier et al. 2007) that would inhibit the efficiency of convection in the stellar envelopes (Mullan & MacDonald 2001). This explanation seems especially plausible given that the closest binary systems are known to show extensive spot coverage (Morales et al. 2009; Windmiller et al. 2010) and strong Hα emission, both of which can be signs of chromospheric activity and strong magnetic fields; similar effects are also seen for young low-mass binaries (e.g., Stassun et al. 2006). These active stars could also yield incorrect radius measurements if the spots are not randomly distributed; Morales et al. (2010) have suggested that concentration of spots near the poles could also explain the discrepancy in measured radii. The most straightforward test of these hypotheses would be to characterize longer-period systems and determine if the mass–radius relation depends on the orbital period (and hence the rotation of the stars). However, this test would require a much larger sample of systems, and is hampered because long-period systems are less likely to eclipse and have a lower eclipse duty cycle (and hence are more difficult to identify and study).

The few known MDEB systems have been discovered serendipitously in programs such as the OGLE microlensing survey, the TReS transiting exoplanet survey, and the Two Micron All Sky Survey (2MASS) calibration field variability

[7] Hubble Fellow.

Table 1
New M-Dwarf Eclipsing Binaries

Name	R.A. (J2000)	Decl.	R_{MG1} (mag)	K_s (mag)	m_{bol} (mag)	μ_α (mas yr^{-1})	μ_δ	σ_μ	SpT
MG1−78457	03 26 20.7	+03 12 36	16.3	12.69	15.38	5	−4	4	M3.3 ± 0.4
MG1−116309	04 48 09.6	+03 17 47	14.9	11.91	14.31	16	10	5	K7.9 ± 0.4
MG1−506664	07 43 11.5	+03 16 22	14.7	11.85	14.35	9	−12	4	M1.0 ± 0.5
MG1−646680	10 30 55.3	+03 34 27	16.0	13.30	15.78	−24	−21	3	M1.0 ± 0.1
MG1−1819499	20 11 51.4	+03 37 20	15.0	12.13	14.63	−18	−33	4	M1.1 ± 0.5
MG1−2056316	23 14 38.3	+03 39 52	14.8	11.64	14.25	−42	−65	4	M2.6 ± 1.1

Notes. The derived properties (m_{bol}, μ, and SpT) were calculated using the multi-catalog data mining procedure we described in Kraus & Hillenbrand (2007). The photometric uncertainties are ∼0.1–0.2 mag for MG1 R, ∼0.02 mag for 2MASS K_s, and ∼0.05 mag for m_{bol}. The R magnitude uncertainty is systematic since it is calibrated into the less well-defined USNOB1.0 R magnitude system. The uncertainty σ_μ is the uncertainty along each axis.

survey (e.g., Maceroni & Montalban 2004; Creevy et al. 2005; Plavchan et al. 2008). There have been searches for MDEBs in existing wide-field variability surveys like ROTSE (Akerlof et al. 2003) and ASAS (Pojmanski et al. 2005), but only one new MDEB has been reported (GU Boo; López-Morales & Ribas 2005) since the shallow depth of these surveys ($V_{lim} \lesssim 13$) limits their sensitivity to intrinsically faint variable stars ($M_V = 9$ for an M0 dwarf, $M_V = 13$ for an M6 dwarf). Any survey to identify a significant number of new MDEBs must extend significantly fainter than current-generation systems while still studying a significant fraction of the sky. To this end, we have launched a program to identify and characterize new MDEBs in deeper variability surveys that are now being released, beginning with the First MOTESS-GNAT survey (MG1; Kraus et al. 2007).

In this paper, we describe the first six M dwarf EB systems to emerge from our search. In Section 2, we briefly outline the discovery of these systems. In Sections 3 and 4, we describe the photometric and spectroscopic observations that contributed to the discovery and analysis of these systems, while in Section 5, we present the analysis that ultimately yields precise masses and radii for the components of each system. Finally, in Section 6, we discuss some of the implications of our updated mass–radius relation for stellar evolutionary models, and we specifically discuss the potential role that stellar rotation plays in determining the mass–radius relation for low-mass stars.

2. DISCOVERY

All six systems were identified in the variability catalog of the First MOTESS-GNAT variable star survey (MG1; Kraus et al. 2007). MG1 is a deep, wide-field imaging survey which was conducted with the Moving Object and Transient Event Search System (MOTESS; Tucker 2007). MOTESS is composed of three 14 inch telescopes which operate in drift-scan mode to conduct deep multi-epoch imaging near the celestial equator. The MG1 survey was compiled from observations taken during the first two years of MOTESS operation and covers a total field of 300 deg^2, with observations of ∼100–120 deg^2 taken twice each night. A total of ∼1.6 million sources were observed at ∼150–250 epochs in this campaign; the MG1 survey identified 26,042 of them to be variable star candidates using the Welch–Stetson variability test (Welch & Stetson 1993).

The observing cadence of MG1 (twice per night for two observing seasons) was too sparse to allow the identification of low-mass EBs by their light curves alone. There are typically 150–250 observations for each source in MG1, so only ∼5–20 observations over an interval of two years will have occurred during an eclipse. Another potential complication is that the observations occurred at intervals of exactly 1 sidereal day, so variability on shorter timescales will be subject to aliasing.

We addressed these issues by disregarding periodicity and light-curve morphology in favor of a more basic diagnostic of possible eclipses: the presence of an excess of faint observations, as determined by the skew of the brightness distribution. This criterion could be biased against the detection of extremely short-period systems (where the eclipse duty cycle is $\gtrsim$50%) because those light curves tend to resemble a balanced sinusoidal shape. However, it is very sensitive to long-period systems (which are otherwise hardest to identify) because their brightness distribution consists of a well-defined Gaussian shape with highly significant outliers. MG1 contains 6061 stars that have light-curve skews of $\geqslant$1, so we narrowed our search to this subset. We then cross-referenced this list of candidates with 2MASS to construct ($R-K$, $J-K$) and ($J-H$, $H-K$) color–color diagrams and selected the 201 candidates with colors consistent with the low-mass main sequence. We further removed all objects with galactic latitude $|b| < 10^\circ$ (to avoid reddened early-type EBs) and visually inspected the remaining curves to remove light curves affected by erroneous measurements, leaving a total of 127 candidates.

As we describe below, we obtained low-resolution optical spectra of these candidates to distinguish true M dwarfs from reddened early-type stars, yielding ∼30 M dwarfs which were likely EBs. Finally, we performed intensive photometric monitoring of each system with small telescopes to confirm its eclipsing nature and establish its period in preparation for detailed follow-up with large-aperture telescopes. As we will report in future publications, we have confirmed at least ∼20 new systems; follow-up for the rest of these systems is ongoing.

We list our newly discovered MDEB systems in Table 1, along with photometry obtained from the discovery survey and from 2MASS (Skrutskie et al. 2006). We also list the proper motion, spectrophotometric distance, bolometric magnitude, and best-fit spectral type as inferred with the astrometric and photometric analysis pipeline described in Kraus & Hillenbrand (2007) and A. L. Kraus et al. (2011, in preparation). This pipeline uses archival astrometry from SDSS, 2MASS, USNO-B1.0, and DENIS to measure the proper motion of a source, then uses the corresponding multicolor photometry to estimate the best-fit spectral type and spectrophotometric distance against a grid of standard spectral energy distributions (SEDs).

3. PHOTOMETRIC OBSERVATIONS

3.1. MG1 Photometry

The MG1 variable star catalog was produced using an automated pipeline that runs in IRAF.[8] Dark subtraction and flat fielding were performed with standard IRAF tasks, and then aperture photometry was measured using the IRAF task QDPhot (Mighell 2000). QDPhot is designed to perform fast photometric analysis for data mining of image archives and is optimized to minimize runtime while still delivering acceptable accuracy and completeness. The primary optimizations are to round the stellar centroid to the nearest pixel and to use only a fixed pattern of whole pixels in the aperture; these choices result in a small increase in uncertainty (∼1%–2%) since the aperture can be offset from the stellar centroid by up to 0.7 pixels.

Differential photometry for each source in MG1 was computed with a modified implementation of inhomogeneous-ensemble differential photometry (IEDP; Honeycutt 1992). In IEDP, all objects are assigned standard magnitudes based on the observations that are taken at darktime with the best seeing and atmospheric transparency. Since all objects have standard magnitudes, they can then all be treated as potential ensemble members. The magnitude offset between the nightly instrumental magnitude and the standard magnitude of each object is then determined by the mean of the difference for an arbitrarily sized ensemble of all objects surrounding it. The internal photometric accuracy for each light curve has been measured to be ∼0.02 mag for the brightest stars ($R \sim 13$–14) and ∼0.04 mag at $R = 16$, which is more than sufficient for the purpose of EB discovery.

All observations reported in MG1 were conducted without a filter to maximize sensitivity, so calibration to a standard photometric system is not easily achieved. We observed that the detector response is well matched by a red photographic plate, so we addressed this challenge by calibrating our final photometric results using the *R*-band photometry of the USNO-A2.0 catalog. The detector response is not a perfect match, which suggests that a small color term is required, plus the original USNO-A2.0 photographic magnitudes are systematically uncertain by ∼0.25 mag, so the photometric calibration should be treated with some caution.

In Table 2, we list the total number of MG1 observations for each object and the standard deviation of all observations obtained outside of the eclipse. The scatter in the light curve is far less than the typical eclipse amplitude, so the eclipse epochs are easily identified. The total number of measurements (∼170–270) was large enough to detect eclipses at 5–20 epochs, but we found that aliasing significantly compromised our effort to measure periods. We therefore decided to obtain additional high-cadence follow-up photometry for our candidate eclipsing systems.

3.2. Follow-up Photometric Monitoring

All of our new MDEBs are relatively bright ($R \sim 15$–16), so we opted to pursue high-cadence follow-up photometry using three small telescopes that could be dedicated to the effort for extended periods of time. Each eclipsing system was observed in an extended campaign until we detected a sufficient number of well-characterized eclipses; we then combined this new data with the existing MG1 data to obtain the additional accuracy afforded by a 6–8 years time baseline. All observations were obtained without filters to maximize sensitivity and because eclipse morphology only changes modestly with color. Systems with periods of <1 day typically yielded the first eclipse within ≲2–3 days and a full period determination within <1 week. Systems with periods of 1.5–2.0 days required a longer observing sequence, but also were typically characterized within <1 week. As we will report in a future publication, we obtained a much longer time series for MG1−2056316 because it is serendipitously located in the same field as another MDEB with a much longer period.

Table 2
Eclipse Timing Observations

MG1−	MG1 Data		Follow-up Data	
	N	σ (mag)	*N*	σ (mag)
78457	168	0.047	291	0.029
116309	185	0.040	289	0.033
506664	192	0.033	153	0.012
646680	222	0.039	334	0.029
1819499	181	0.028	220	0.025
2056316	120	0.044	876	0.021

The first monitoring system, co-located with MOTESS outside Tucson and operated by R. Tucker, consists of a Celestron 8 telescope with an Edward Byers worm-gear-driven mounting and an SBIG ST9 imaging camera. This system is manually operated but capable of unattended tracking and imaging of a field of interest all night. Data acquisition, processing of the collected images, and photometric reduction were accomplished with Maxim DL.

The other two monitoring systems are operated by M. Thompson. The first system, located in New Mexico, is a 16″ RC Optical Systems Ritchey–Chretien OTA on a Bisque Paramount ME robotic mount and uses an SBIG STL-6303E camera. The second system, located in Northern California, is a 14″ Meade SCT OTA on another Bisque Paramount ME mount and uses an SBIG STL-1301E camera. These systems are fully automated using a combination of custom-written software and the packages CCDsoft and TheSky6, both by Bisque. All data were processed using a mix of custom-written software and Maxim DL for image calibration, plus Mira Pro for aperture photometry.

As for the discovery observations from MG1, we list the total number of follow-up observations for each target and the standard deviation of all non-eclipse observations in Table 2.

3.3. Multicolor Eclipse Photometry

The geometry of an EB system is simple, so approximate values for the component temperatures and radii can be obtained from basic light-curve properties such as the eclipse duration or the primary and secondary eclipse depths. However, precise estimation of radii and temperatures requires detailed modeling to account for the inclination and limb darkening. Our discovery and timing observations were obtained with small telescopes using unfiltered data, so those data do not have sufficient precision, time cadence, or color information to serve this purpose. We instead addressed this requirement by obtaining updated light curves of each system's primary and secondary eclipse using the roboticized Palomar 60″ telescope (P60; Cenko et al. 2006).

The P60 operates solely as an optical imager and is controlled by an automated queue-scheduling routine. Its camera has a

[8] IRAF is distributed by the National Optical Astronomy Observatory, which is operated by the Association of Universities for Research in Astronomy, Inc., under cooperaive agreement with the National Science Foundation.

Table 3
Multicolor Eclipse Observations

MG1−	Primary Eclipse						Secondary Eclipse					
	N_{obs}	Epoch (JD − 2450000)	Duration (hr)	σ_I (mag)	σ_R (mag)	σ_V (mag)	N_{obs}	Epoch (JD − 2450000)	Duration (hr)	σ_I (mag)	σ_R (mag)	σ_V (mag)
78457	90	4758.92	3.05	0.009	0.016	0.029	94	4781.92	3.09	0.013	0.039	0.077
116309	72	4783.81	3.08	0.016	0.015	0.028	53	4547.66	1.68	0.008	0.008	0.011
506664	75	4573.73	2.64	0.007	0.009	0.013	68	4580.70	2.17	0.009	0.010	0.018
646680	76	4547.83	2.44	0.013	0.025	0.053	78	4579.77	2.49	0.021	0.049	0.071
1819499	80	4738.75	3.01	0.011	0.018	0.014	89	4739.69	3.09	0.006	0.008	0.013
2056316	94	4730.79	3.03	0.006	0.009	0.013	93	4755.77	2.95	0.006	0.015	0.012

Note. The photometric uncertainties σ for each observation were estimated from the scatter in the observations taken before and/or after each eclipse.

field of view of 11′ and a pixel scale of 0.″378 pixel^{-1}, but we operated in a 5.5 × 11′ subarray in order to reduce the read time to ∼15 s, matching our very short exposures. Each monitoring window was set 1 hr wider than the eclipse to obtain constant (non-eclipse) observations and to allow for some flexibility in the queue-scheduling software. However, our observations were sometimes interrupted by weather or higher-priority events, so some observations were truncated and do not include post-eclipse brightness measurements. Our observation sequence used alternating exposures with *VRI* filters to obtain coeval three-color light curves. In all cases, we used exposure times of 30 s in *V* and 15 s in *R* and *I*, so the interval between subsequent observations in the same filter is 107 s.

All images from the P60 are automatically bias-subtracted and flat-fielded as part of the data acquisition pipeline. We extracted magnitudes for all of the stars in these images using the IRAF task PHOT, which is part of the DAOPHOT package (Stetson 1987), and then we measured differential photometry for each MDEB with respect to several bright, constant check/comparison stars. Our science targets are somewhat redder than the typical comparison stars, so we tested for an airmass-dependent color term in the differential photometry, but found no evidence that one was needed at the level of our photometric precision. Finally, we compared the MDEB brightness from before and after each eclipse to test for systematic effects or secular changes in brightness due to star spots, but found little evidence for spot-driven brightness variations at a level of $\gtrsim$1%.

In Table 3, we list the total number of observations per filter for each eclipse window, the duration of the time series, and the estimated photometric precision. In Table 4, we list the 2833 brightness measurements from our P60 observations.

Table 4
Multicolor Eclipse Data

MG1−	Filter	HJD − 2450000	ΔM[a] (mag)	σ_M (mag)
78457	*I*	4758.876471	−0.008	0.010
78457	*I*	4758.877802	0.001	0.009
78457	*I*	4758.879133	0.005	0.009
78457	*I*	4758.880463	0.008	0.014
78457	*I*	4758.881794	0.020	0.009
78457	*I*	4758.883124	0.039	0.010
78457	*I*	4758.884458	0.052	0.010
78457	*I*	4758.885789	0.065	0.010
78457	*I*	4758.887120	0.068	0.009
78457	*I*	4758.888451	0.067	0.009

Notes.
[a] All differential magnitudes are reported with respect to the average of all measurements taken outside of the eclipse, such that the magnitude outside of eclipse is $M = 0$.
[b] The photometric uncertainties for each observation correspond to the photon counting statistics for the source and background. In our light-curve fits, we replaced this measurement with the observed scatter outside of eclipse (Table 3) if the observed scatter was larger, indicating that other noise sources dominated.

(This table is available in its entirety in a machine-readable form in the online journal. A portion is shown here for guidance regarding its form and content.)

4. SPECTROSCOPIC OBSERVATIONS

4.1. Long-slit Spectroscopy

As part of our selection process, we obtained moderate resolution optical spectra from our new MDEB systems. These spectra were intended to distinguish genuine low-mass EB systems from various types of interlopers, but they can also be used to estimate the temperature, surface gravity, chromospheric activity, and (approximate) metallicity of the systems.

All of our spectra were obtained with the Double Spectrograph (Oke & Gunn 1982) on the Hale 5 m telescope at Palomar Observatory. Spectra presented here were obtained with the red channel using a 316 l mm^{-1} grating and a 2.″0 slit, yielding a spectral resolution of $R \sim 1250$ over a wavelength range of 6400–8800 Å. Wavelength calibration was achieved by observing a standard lamp after each science target, and flux normalization was achieved by periodic observation of spectrophotometric standard stars from the compilation of Massey et al. (1988). All spectra were dark-subtracted and flat-fielded using standard IRAF routines, and then the stellar spectra were extracted using the IRAF routine APALL. Finally, wavelength calibration and continuum normalization were conducted using standard IRAF routines.

We list the epochs and exposure times in Table 5. Most of the spectra have S/N > 50, but the data for MG1−646680 are much noisier since it was observed in marginal conditions; we did not re-observe it because its quality was sufficient for spectral typing based on the broad TiO absorption bands.

4.2. Echelle Spectroscopy

In order to estimate the masses of our targets, we must measure the radial velocity (RV) curves of the individual component stars of each system. In a system with two 0.5 $M_\odot$ stars in a one day orbit, the orbital velocity of each star with respect to the other will be ∼200 km s^{-1}. We therefore must acquire high-dispersion spectra with velocity resolutions significantly lower than this value. Single-order spectrographs can achieve the required precision, but the preferred solution is to

Table 5
Low-resolution Spectroscopic Observations

MG1−	Epoch (JD − 2450000)	t_{int} (s)	SpT	EW(Hα) (Å)	TiO_{7140}	TiO_{8465}	Na_{8189}	TiO_5	CaH_2
78457	4083.72	300	M3.5	−6.5	1.69	1.12	0.85	0.46	0.51
116309	4083.75	300	M0.5	−2.9	1.15	1.02	0.93	0.79	0.72
506664	4084.03	420	M1.0	−2.0	1.30	1.03	0.91	0.61	0.59
646680	3906.66	300	M1.0	−3.3	1.23	1.00	0.92	0.56	0.55
1819499	3889.97	120	M0.5	−2.7	1.24	0.98	0.96	0.73	0.70
2056316	4083.66	300	M2.5	−2.3	1.46	1.06	0.87	0.52	0.49

use echelle spectrographs that sample a much wider wavelength range by observing many orders of the spectra at once.

We obtained our high-dispersion spectra using the High-Resolution Echelle Spectrometer (HIRES) on the Keck-I 10 m telescope. HIRES is a single-slit echelle spectrograph permanently mounted on the Nasmyth platform of Keck 1. All observations were performed using the red channel of HIRES, and most span a wavelength range of 5300–9900 Å. All observations were obtained using the C2 or D1 deckers, which feature slit widths of 3 or 4 pixels; the corresponding spectral resolutions are $R \sim 45{,}000$ or $R \sim 36{,}000$. We processed our HIRES data using the standard extraction pipeline MAKEE,[9] which automatically extracts, flat-fields, and wavelength-calibrates spectra taken in most standard HIRES configurations.

In Table 6, we list the epochs and exposure times for all of our HIRES observations, as well as the S/N for each spectrum at 6600 Å. Due to the wide wavelength coverage in a typical echelle spectrum, RVs can typically be measured even when individual spectral lines are measured only at S/N $\lesssim$ 3. However, we obtained most of our observations at much higher S/N in order to allow future measurement of individual line strengths, once suitable calibrations for properties such as metallicity and surface gravity become available. As we show in Section 5.3, this choice also allows us to achieve excellent precision in our final RV measurements despite only having a small number of epochs. Two of our observing runs suffered from poor weather, so our phase coverage for some systems is not as even or dense as we would prefer. However, most systems with periods of $\lesssim$7 days should tidally circularize within $\lesssim$1 Gyr (e.g., Mathieu et al. 2004 and references therein), so we should only need two epochs (yielding four RVs) to constrain the three observational free parameters for each system: the RV curve amplitudes K_A and K_B, plus the mean RV of the system. All additional epochs only serve to reduce the uncertainties as $\sqrt{N_{obs}}$ and to test for systematic noise due to spots, flares, and instrumental effects. They are also valuable in confirming that the orbits are truly circular.

During each sequence of observations, we also observed late-type stars from the list of RV standards compiled by Nidever et al. (2002). These standard stars were chosen to simultaneously serve as RV standards and as fitting templates for our analysis of the MDEB spectra. We also observed a large number of FGK stars during twilight in order to further calibrate the RVs between nights. We list the K7–M4 standard stars that we used in Table 7. As was discussed by Nidever et al., even though these targets are RV stable at $\lesssim$0.1 km s^{-1} over a timescale of a few years, the absolute RVs are likely to be systematically uncertain by $\sim$0.4 km s^{-1} at late spectral types.

We found that even when the instrument configuration is left unchanged, the velocity calibration can vary by $\sim$1 km s^{-1} over the course of a night. We have corrected this velocity drift in each observation by cross-correlating its telluric features (using the IDL *c_correlate* function) at 7600 Å and 9300 Å with the corresponding bands in five RV standards (GJ 450, GJ 908 (first epoch), GJ 408, HD 285968 (first epoch), and GJ 109) that appear to have zero velocity drift with respect to each other and to the average of all 20 remaining RV standards.

After applying the telluric RV correction, we cross-correlated all of our RV standards with each other in order to determine the intrinsic RV uncertainty for bright, slow-rotating M dwarfs. We found that the scatter for cross-correlations between pairs of spectra is $\sim$450 m s^{-1}, indicating that each spectrum has an intrinsic velocity uncertainty of $\sim$300 m s^{-1}. This measurement uncertainty is seen even between separate observations of the same targets, so it seems to be caused by astrophysical or instrumental effects, not uncertainties in the measurements by Nidever et al. As we discuss in Section 5.3, we have calibrated each of our science observations with the $\sim$10 standard stars within $\pm$1 spectral subtype in order to reduce the calibrators' contribution to the error budget to $\sim$100 m s^{-1}; this contribution is small compared to the 300 m s^{-1} contribution from the science observations themselves, yielding total uncertainties of $\sim$350 m s^{-1}.

5. ANALYSIS AND RESULTS

Our data analysis can be divided into several major stages, which we describe in the following subsections. First, we analyzed the moderate-resolution spectra of each system in order to characterize their atmospheric properties and confirm that they should have component masses $M \lesssim 0.6\,M_\odot$. Next, we combined all of the time-series photometry of our systems in order to measure their orbital periods and eclipse timing. After this, we analyzed the high-dispersion spectra of each system in order to measure their RV curves and component masses (modulo inclination). Finally, we analyzed the multicolor eclipse light curves of our systems in order to measure the components' masses, radii, and temperatures.

5.1. Spectral Types and Emission Line Strengths

The moderate-resolution spectra yield spectral types that allow us to determine temperatures in a way that is independent of our broadband SED fitting (Section 2). Furthermore, the depths of alkaline absorption lines can demonstrate low surface gravity indicative of youth (Slesnick et al. 2006a), and the relative strengths of molecular bands (e.g., metal hydride versus metal oxide) distinguish metal-poor subdwarfs from solar-metallicity dwarfs (Woolf & Wallerstein 2006).

In Figure 1, we plot the flux-normalized spectra for each of the new systems. We estimated spectral types via qualitative comparison of each spectrum to a range of standard stars from

[9] http://spider.ipac.caltech.edu/staff/tab/makee

Table 6
High-resolution Spectroscopic Observations

MG1−	Epoch (HJD − 2400000)	Phase	t_{int} (s)	S/N (6600 Å)	v_{prim} (km s^{-1})	v_{sec} (km s^{-1})	EW(Hα)$_{prim}$ (Å)	EW(Hα)$_{sec}$ (Å)
78457	54484.89201	0.2453	900	6	−62.68	120.90	−2.99	−1.80
78457	54485.87340	0.8640	900	7	92.02	−46.23	−2.60	−1.70
78457	54485.93567	0.9033	900	6	75.65	−28.45	−2.77	−1.73
78457	54688.04238	0.3185	900	12	−55.10	111.45	−2.53	−1.91
78457	54688.09510	0.3518	900	13	−45.43	101.29	−2.13	−1.80
78457	54691.03629	0.2060	900	11	−59.29	116.88	−2.31	−1.89
78457	54691.09811	0.2450	900	10	−63.20	120.34	−2.47	−2.17
78457	54692.03966	0.8386	900	7	100.47	−55.44	−2.59	−1.85
78457	54692.10596	0.8804	900	6	86.32	−39.01	−2.46	−1.74
116309	54467.86931	0.0319	900	15	30.73	81.57	...	...
116309	54483.79741	0.2887	900	29	−54.34	173.11	−0.83	−1.28
116309	54483.83669	0.3362	900	32	−41.58	158.92	−0.88	−1.31
116309	54483.86564	0.3712	900	20	−25.58	143.52	−0.82	−1.32
116309	54485.92519	0.8611	900	26	142.45	−36.54	−0.91	−1.39
116309	54688.10473	0.2924	900	32	−53.75	172.23	−0.89	−1.24
116309	54691.13373	0.9544	900	23	86.78	20.17	...	...
116309	54692.12727	0.1556	900	17	−38.01	156.24	−0.92	−1.05
506664	54468.00623	0.7214	815	7	77.84	−111.26	−1.08	−0.91
506664	54468.01895	0.7299	900	12	77.95	−111.40	−0.94	−0.99
506664	54483.85152	0.9547	900	25	12.65	−40.87	...	...
506664	54485.96523	0.3198	900	26	−96.85	76.39	−1.15	−0.98
506664	54486.02658	0.3594	900	27	−84.73	63.31	−1.16	−0.93
506664	54486.07599	0.3913	900	24	−71.58	49.44	−1.11	−1.05
506664	54486.12058	0.4201	900	18	−57.87	34.67	−1.28	−1.19
646680	54466.99903	0.6358	1200	10	121.59	−11.73	−0.95	−0.63
646680	54467.16147	0.7350	1200	6	142.13	−35.09	−1.49	−0.81
646680	54485.95185	0.2098	900	13	−21.64	149.38	−1.58	−0.88
646680	54486.03798	0.2624	900	13	−24.24	151.82	−1.48	−0.77
646680	54486.10776	0.3050	900	14	−19.43	146.74	−1.18	−0.77
646680	54486.14463	0.3275	900	13	−14.51	141.36	−1.20	−0.79
1819499	54687.79186	0.1596	900	28	−124.05	90.63	−1.03	−0.99
1819499	54687.83039	0.2207	900	27	−141.40	108.04	−0.89	−0.97
1819499	54687.87370	0.2894	900	30	−139.30	107.20	−1.05	−0.99
1819499	54688.06275	0.5893	900	26	48.11	−87.91	−1.17	−1.12
1819499	54690.76360	0.8742	900	31	70.34	−111.34	−1.15	−1.40
1819499	54690.82930	0.9785	900	27	8.66	−38.70	...	...
1819499	54690.92684	0.1332	900	25	−110.93	77.40	−1.10	−1.19
1819499	54690.96773	0.1981	900	26	−137.02	104.04	−0.87	−0.96
1819499	54691.00505	0.2573	900	23	−143.14	110.50	−1.02	−1.01
1819499	54691.84209	0.5853	900	29	45.12	−86.06	−0.82	−1.07
1819499	54691.91316	0.6980	900	25	99.33	−142.97	−0.94	−1.08
1819499	54691.96015	0.7726	900	24	105.28	−147.06	−1.22	−1.26
2056316	54687.94116	0.1300	900	28	−58.51	63.69	−1.97	−0.90
2056316	54687.99439	0.1609	900	31	−67.79	74.56	−1.89	−0.85
2056316	54688.08689	0.2146	900	30	−77.42	86.45	−1.74	−0.83
2056316	54688.12519	0.2368	900	30	−78.95	88.52	−1.65	−0.75
2056316	54690.90102	0.8480	900	22	57.91	−79.25	−1.76	−0.94
2056316	54690.95446	0.8790	900	24	48.04	−67.49	−1.66	−0.92
2056316	54690.99224	0.9009	900	23	40.30	−57.81	...	...
2056316	54691.86303	0.4064	900	24	−45.41	47.66	−1.65	−0.88

the work of Slesnick et al. (2006a, 2006b), who used the same instrument configuration. We confirmed these estimates by calculating the spectral indices TiO-7140 and TiO-8465, which measure the depth of key temperature-sensitive features (Slesnick et al. 2006a). We find that these indices are consistent with our assigned spectral types, but this only provides a strong constraint for sources with types of $\gtrsim$M2 stars since both indices saturate for types earlier than ∼M1.

Our SED-fit spectral types are consistent with the spectroscopic spectral types, but typically more precise, so we used the SED-fit measurements to determine the effective temperatures for each component of each binary. For each system, we first used our composite spectral type (which represents the average of both components) to estimate a composite temperature from the temperature scale we reported in Kraus & Hillenbrand (2007). We then specifically estimated the component temperatures using the temperature ratio we inferred in Section 5.4, assuming that the composite temperature represented an average of the two component temperatures that was weighted by their respective contributions to the total system luminosity.

We also measured the equivalent width of Hα emission, a measure of chromospheric activity. As we discuss in Section 5.3, all of our targets show Hα emission, matching the ubiquity seen for most short-period spectroscopic binaries. However,

Table 7
RV/SpT Calibrators

Name	SpT	Epoch (HJD − 2400000)	v (km s^{-1})	S/N (6600 Å)
GJ 156	K7	54690	62.6	260
HD 28343	K7	54691	−35.1	85
HD 95650	M0	54485	−13.9	260
GJ 678.1A	M0	54691	−12.5	130
GJ 96	M0.5	54484	−37.9	300
GJ 908	M1	54466	−71.1	70
GJ 450	M1	54485	0.3	230
HD 165222	M1	54687	32.7	240
GJ 908	M1	54690	−71.1	270
HD 165222	M1	54691	32.7	140
HD 36395	M1.5	54485	8.7	340
HD 36395	M1.5	54687	8.7	250
HD 216899	M1.5	54691	−27.3	160
GJ 2066	M2	54467	62.2	55
HD 285968	M2.5	54467	26.2	110
GJ 408	M2.5	54485	3.2	220
HD 180617	M2.5	54687	35.9	250
HD 180617	M2.5	54691	35.9	140
HD 285968	M2.5	54691	26.2	70
HD 173739	M3	54690	−0.8	160
GJ 109	M3.5	54484	30.6	190
HD 173740	M3.5	54690	1.2	100
GJ 628	M3.5	54691	−21.2	100
GJ 447	M4	54485	−31.1	130
GJ 699	M4	54691	−110.5	130

Notes. Velocities were adopted from the list of standard stars reported by Nidever et al. (2002), who found that they have internal dispersion of $\lesssim$0.1 km s^{-1} and systematic uncertainties of $\lesssim$0.4 km s^{-1}. Spectral types were adopted from the PMSU surveys (e.g., Reid et al. 1995).

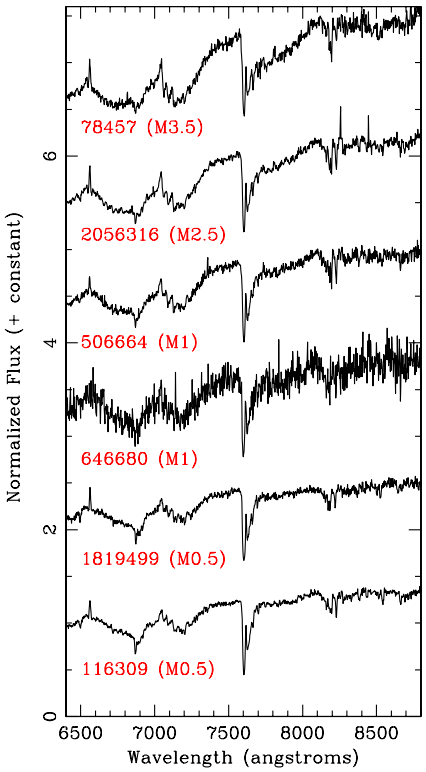

Figure 1. Intermediate-resolution spectra for our six new MDEB systems. The TiO band at 7100 Å is clearly present in all spectra, suggesting spectral types of M0 or later. Most of them also show some evidence of Hα emission, which indicates either youth or chromospheric activity. None possess the shallow Na-8189 doublet that is characteristic of young systems and most are not near regions of ongoing star formation, so the Hα emission seems to result from as the high activity common to close binary systems. The spectrum of MG1−646680 is noisier, despite its longer integration time, because it was observed in marginal conditions.

(A color version of this figure is available in the online journal.)

the emission was not always strong enough to be measured in these lower-resolution spectra, especially for targets which were observed at low S/N. Finally, we measured the gravity-sensitive spectral index Na_{8189} (Slesnick et al. 2006a) and the metallicity-sensitive spectral indices TiO_5 and CaH_2 (Woolf & Wallerstein 2006). In all cases, these spectral indices are consistent with dwarf gravity and near-solar metallicity.

We summarize all of these measurements in Table 5.

5.2. Eclipse Timing

Our photometric observations span an interval of ∼7 years, so simultaneous analysis of all data should yield very precise measurements of the orbital periods (P). The fast cadence and high precision of the P60 observations should also allow us to estimate the time of eclipse (t_0) very precisely. However, our data is heterogeneous and represents several different telescopes and filter systems, so our analysis proceeds through several steps in order to achieve this result. Our final results show that the measurement of t_0 is set entirely by our data from the P60, while the measurement of P is set by that value of t_0 and by the eclipse epochs in our MG1 and small-telescope follow-up data.

For each system, we first used the period analysis package PERANSO[10] to analyze the light curve from our small telescope follow-up observations, measuring the orbital period with a precision of $\lesssim$0.01 days and establishing a provisional primary eclipse epoch with a precision of ∼2–5 minutes. This step was critical because aliasing and sparse time coverage made it impossible to determine unambiguous periods from MG1 data alone, and we required those periods to plan all subsequent follow-up observations. After determining provisional values, we then exploited the much longer time baseline of the MG1 light curves (both alone and in combination with our follow-up data) to refine our estimate of each system's period with a precision of $\lesssim 10^{-5}$ days. We also used these updated values to plan optimal follow-up observations with the P60. Finally, we used the P60 eclipse light curves to establish a final value of t_0, and then reanalyzed the MG1 and small-telescope data with this fixed value of t_0 in order to measure a final value for the orbital period (with a precision of $\sim 10^{-6}$ days).

We summarize our final periods and eclipse epochs for each system in Table 8, and in Figures 2–6 we show the final phased light curves for MG1 observations (Figure 2), our small telescope follow-up (Figure 3), and the P60 multicolor observations (Figures 4–6). We found that the typical uncertainty in the P60 eclipse timing (as determined from the dispersion between filters and between the primary and secondary eclipses) is ∼10–20 s ($\sigma_{t0}/P \sim 10^{-4}$), while the uncertainties in the periods are ∼0.05–0.3 s ($\sigma_P/P \sim 10^{-6}$–10^{-7}). Even though the eclipse timing from the earliest observations has relatively modest accuracy (∼5–10 minutes), the corresponding period is still very precise since the uncertainty in the period declines with the inverse of the number of periods that our data set spans (typically $\gtrsim$2000–5000).

[10] http://www.peranso.com/

Table 8
System Properties

Parameter	Units	MG1 − 78457	MG1 − 116309	MG1 − 506664	MG1 − 646680	MG1 − 1819499	MG1 − 2056316
Light-curve Timing							
P	(Days)	1.5862046 ± 0.0000008	0.8271425 ± 0.0000004	1.5484492 ± 0.0000006	1.6375302 ± 0.0000015	0.6303135 ± 0.0000002	1.7228208 ± 0.0000042
$T_{0,\mathrm{avg}}$	(HJD − 2450000)	4758.91630 ± 0.00010	4783.81137 ± 0.00003	4573.73166 ± 0.00003	4547.83444 ± 0.00008	4738.74669 ± 0.00004	4730.78778 ± 0.00004
$T_{0,\mathrm{prim}}$	(HJD − 2450000)	4758.91610 ± 0.00014	4783.81125 ± 0.00006	4573.73148 ± 0.00004	4547.83414 ± 0.00010	4738.74670 ± 0.00006	4730.78802 ± 0.00006
$T_{0,\mathrm{sec}}$	(HJD − 2450000)	4781.91647 ± 0.00013	4547.66231 ± 0.00003	4580.69986 ± 0.00004	4579.76658 ± 0.00013	4739.69215 ± 0.00004	4755.76843 ± 0.00006
Radial Velocity Orbital Parameters							
$\bar{v}$	(km s^{-1})	25.48 ± 0.09	55.83 ± 0.15	−13.31 ± 0.11	58.77 ± 0.12	−18.82 ± 0.08	−3.75 ± 0.10
K_A	(km s^{-1})	88.41 ± 0.16	113.31 ± 0.23	92.33 ± 0.20	83.25 ± 0.18	124.79 ± 0.13	75.43 ± 0.17
K_B	(km s^{-1})	94.93 ± 0.16	120.75 ± 0.23	99.22 ± 0.20	93.64 ± 0.18	129.86 ± 0.14	92.53 ± 0.18
$M_{\mathrm{tot}} \sin^3(i)$	($M_\odot$)	1.0126 ± 0.0036	1.0986 ± 0.0045	1.1273 ± 0.0049	0.9388 ± 0.004	1.0781 ± 0.0024	0.846 ± 0.004
$M_A \sin^3(i)$	($M_\odot$)	0.524 ± 0.002	0.567 ± 0.002	0.584 ± 0.002	0.497 ± 0.002	0.550 ± 0.001	0.466 ± 0.002
$M_B \sin^3(i)$	($M_\odot$)	0.488 ± 0.001	0.532 ± 0.002	0.543 ± 0.002	0.442 ± 0.002	0.528 ± 0.001	0.380 ± 0.001
q	(M_B/M_A)	0.931 ± 0.002	0.938 ± 0.003	0.931 ± 0.003	0.889 ± 0.003	0.961 ± 0.002	0.815 ± 0.003
$a \sin(i)$	($R_\odot$)	5.749 ± 0.007	3.827 ± 0.005	5.864 ± 0.009	5.726 ± 0.008	3.173 ± 0.002	5.721 ± 0.009
Light-curve-fitting Parameters							
i	(deg)	86.78 ± 0.05 ± 0.06	88.74 ± 0.07 ± 0.20	88.9 ± 0.02 ± 0.09	87.21 ± 0.04 ± 0.07	84.77 ± 0.04 ± 0.12	86.08 ± 0.02 ± 0.05
ΔT_{eff}	(K)	64 ± 6 ± 8	106 ± 2 ± 10	119 ± 1 ± 8	104 ± 6 ± 14	83 ± 2 ± 14	136 ± 3 ± 10
$T_{\mathrm{eff,A}}$[a]	(K)	3330 ± 60	3920 ± 80	3730 ± 90	3730 ± 20	3690 ± 80	3460 ± 180
$T_{\mathrm{eff,B}}$[a]	(K)	3270 ± 60	3810 ± 80	3610 ± 90	3630 ± 20	3610 ± 80	3320 ± 180
R_A	($R_\odot$)	0.505 ± 0.008 ± 0.007	0.552 ± 0.004 ± 0.013	0.560 ± 0.001 ± 0.004	0.457 ± 0.006 ± 0.004	0.569 ± 0.002 ± 0.023	0.441 ± 0.002 ± 0.002
R_B	($R_\odot$)	0.471 ± 0.009 ± 0.007	0.532 ± 0.004 ± 0.008	0.513 ± 0.001 ± 0.008	0.427 ± 0.006 ± 0.002	0.500 ± 0.003 ± 0.014	0.374 ± 0.002 ± 0.002
a	($R_\odot$)	5.758 ± 0.014	3.828 ± 0.011	5.865 ± 0.017	5.733 ± 0.016	3.186 ± 0.005	5.734 ± 0.017
M_A	($M_\odot$)	0.527 ± 0.002	0.567 ± 0.002	0.584 ± 0.002	0.499 ± 0.002	0.557 ± 0.001	0.469 ± 0.002
M_B	($M_\odot$)	0.491 ± 0.001	0.532 ± 0.002	0.544 ± 0.002	0.443 ± 0.002	0.535 ± 0.001	0.382 ± 0.001
Spectroscopic Parameters							
EW(Hα)$_{\mathrm{prim}}$	(Å)	−2.54 ± 0.08	−0.87 ± 0.04	−1.12 ± 0.11	−1.31 ± 0.24	−1.02 ± 0.13	−1.77 ± 0.12
EW(Hα)$_{\mathrm{sec}}$	(Å)	−1.84 ± 0.05	−1.31 ± 0.06	−1.01 ± 0.10	−0.78 ± 0.08	−1.09 ± 0.14	−0.86 ± 0.06

Note.
[a] Temperature uncertainties are inferred from the uncertainty in the SED-fit spectral type (Section 2) and from the temperature scale reported in Kraus & Hillenbrand (2007). Any temperatures inferred from such a scale should be regarded as systematically uncertain by ∼50–100 K. The uncertainty for MG1−646680 is smaller than the rest because its SED fit includes very precise SDSS *ugriz* magnitudes.

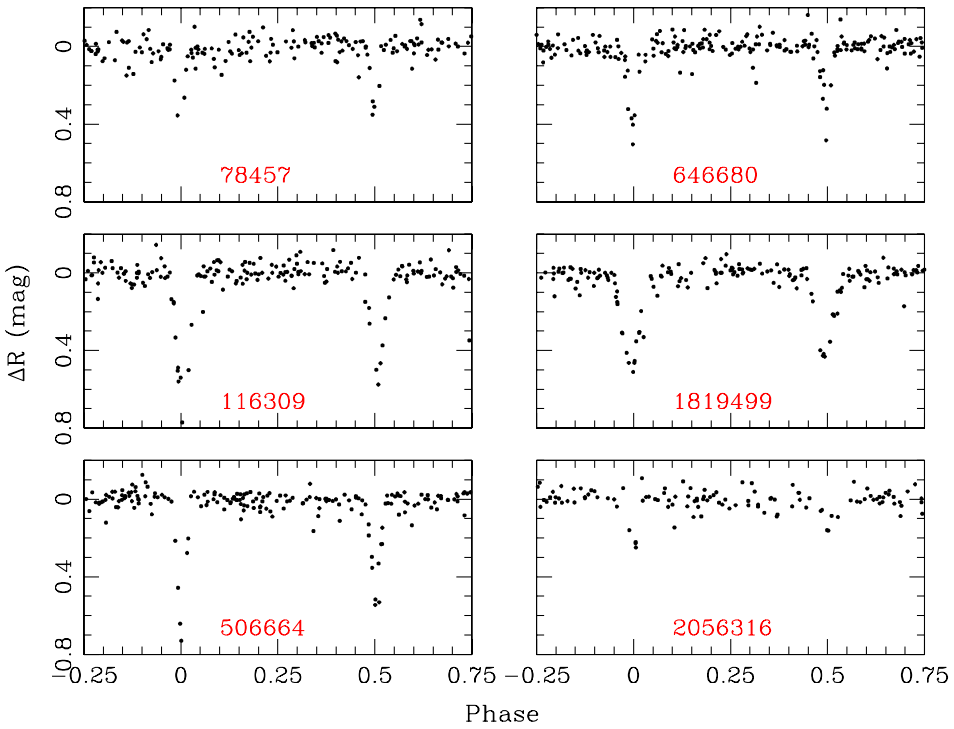

Figure 2. Phased discovery light curves for our systems, as measured with the MOTESS telescopes. All of the systems showed evidence of eclipses in the unphased light curves, but the discovery light curves did not have a sufficient number of points to determine an unambiguous period.

(A color version of this figure is available in the online journal.)

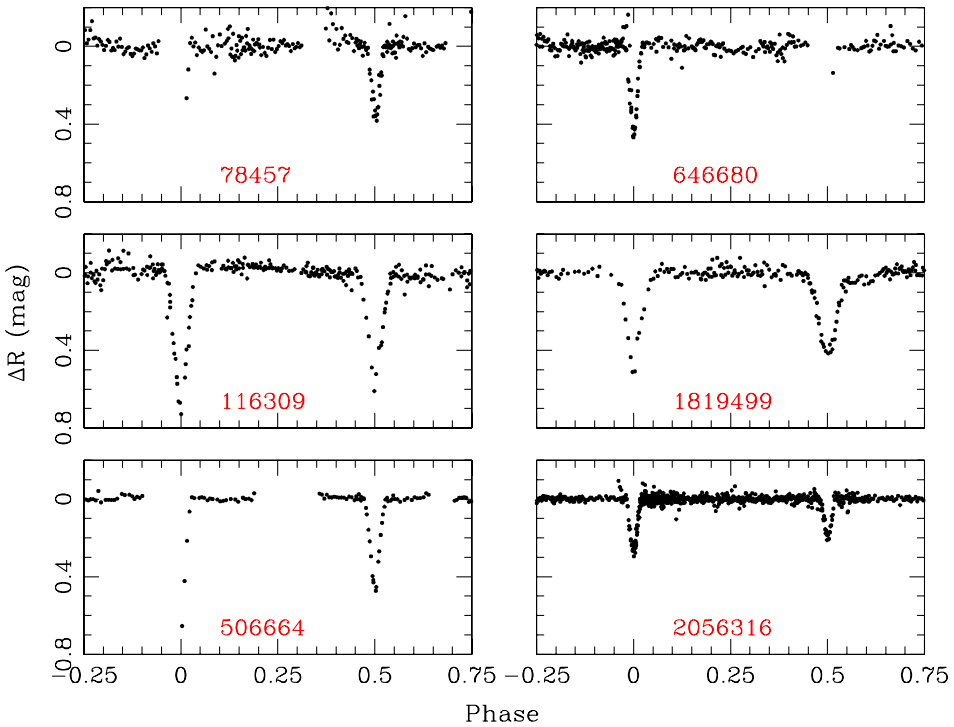

Figure 3. Phased follow-up light curves for our systems as measured with several small telescopes. These observations typically spanned several whole nights in a row, and the detection of several consecutive eclipses allowed us to determine each system's actual period; we then combined this data with our MG1 observations to determine the system periods and eclipse epochs needed for additional follow-up observations.

(A color version of this figure is available in the online journal.)

5.3. Radial Velocities

There are several methods commonly used to analyze high-dispersion spectra and measure RVs, including the cross-correlation, two-dimensional correlation (TODCOR; Mazeh & Zucker 1994), and broadening function deconvolution (BF; Rucinski 1999). We have chosen to analyze our data using BF; as Rucinski described, BF is less susceptible to effects like "peak pulling" than correlation techniques, especially for targets like ours where the cross-correlation peaks are

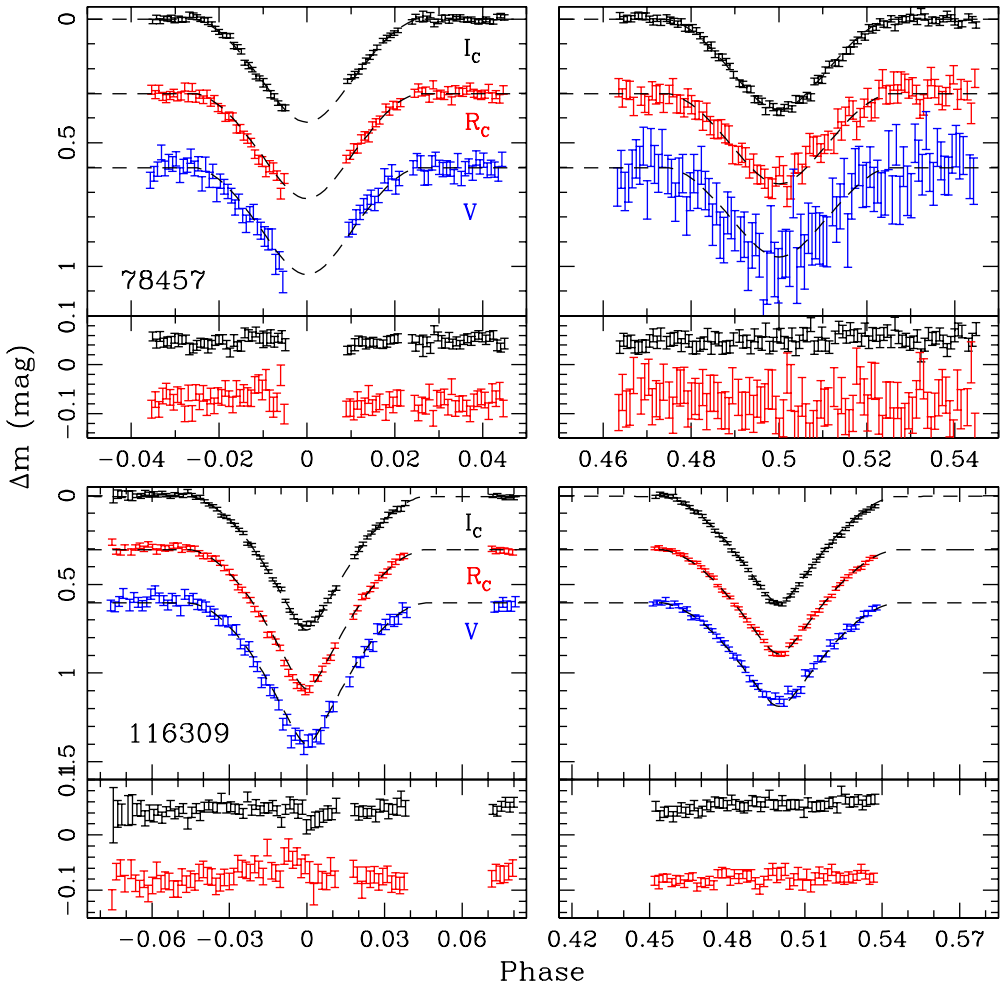

Figure 4. Multicolor eclipse light curves for two of our newly discovered M dwarf EB systems: MG1−78457 and MG1−116309. For each system, we show the light curves in I_C (black), R_C (red), and V (blue), as well as the predicted light curves from our best-fit radius models (dashed lines). The R_C and V observations were offset to avoid overlap. Below each plot, we show the residuals in I_C and R_C with an expanded scale in order to demonstrate the typical scatter; we do not show the residuals for V in order to avoid crowding the plot and because the typical scatter can be discerned adequately without an expanded scale. As we discuss in the text, a flare was seen in the middle of the secondary eclipse for MG1−78457; we have omitted those data points in fitting our light-curve models.

(A color version of this figure is available in the online journal.)

broadened by rotation and might partially overlap. S. Rucinski distributes an IDL pipeline that is designed to conduct BF for any input spectrum,[11] and we adopted this pipeline as written.

For each order of each spectrum, we used the BF pipeline to calculate the broadening function with respect to a bright RV standard star of similar spectral type. We then fit the two peaks of the broadening function with a pair of Gaussian functions in order to measure the component RVs for that order, and measured the average component RVs for that epoch by calculating a weighted mean of all orders. We estimated those weights by iteratively calculating the weighted mean RVs for all observations, measuring the standard deviation of each order's residuals around those averages, and using the standard deviations to update the weight assigned to each order. We started by assigning all orders an equal weight, and then iterated until the weights and the average component RVs converged. Finally, we repeated this process for all RV standards within ±1 spectral subclass of the science target (Table 5), and averaged the resulting RVs at each epoch in order to minimize systematic uncertainties in the RV calibration. A typical cross-correlation to a single standard incurs velocity errors of ∼300 m s^{-1} from the science target and ∼300 m s^{-1} from the RV standard, but by using ∼10 RV standards, we can reduce the second contribution to a negligible ∼100 m s^{-1}. We find that the scatter of our measurements around the RV orbit fits is ∼300 m s^{-1}; including degrees of freedom that contribute to the fit, then the inferred uncertainties are ∼350 m s^{-1}, which is consistent with our estimate.

In Figure 7, we demonstrate the steps of this process by plotting one echelle order for an observation of MG1−116309, the corresponding echelle order of one RV template star, the broadening function that relates the standard star spectrum to the spectrum of MG1−116309, and the RV residuals as a function of wavelength for each order of that spectrum (as determined from all epochs). Despite the significant rotational broadening seen for both components of MG1−116309, the order shown (and many other orders) yield measurements with an individual precision of ∼1–2 km s^{-1}. However, many of the orders suffer from severely degraded precision; this is typically a sign that those orders have fewer deep spectral lines than the orders that offer better precision. We list the component RVs (as averaged over all orders, and then over all RV standards) for each epoch in Table 6.

[11] http://www.astro.utoronto.ca/∼rucinski/

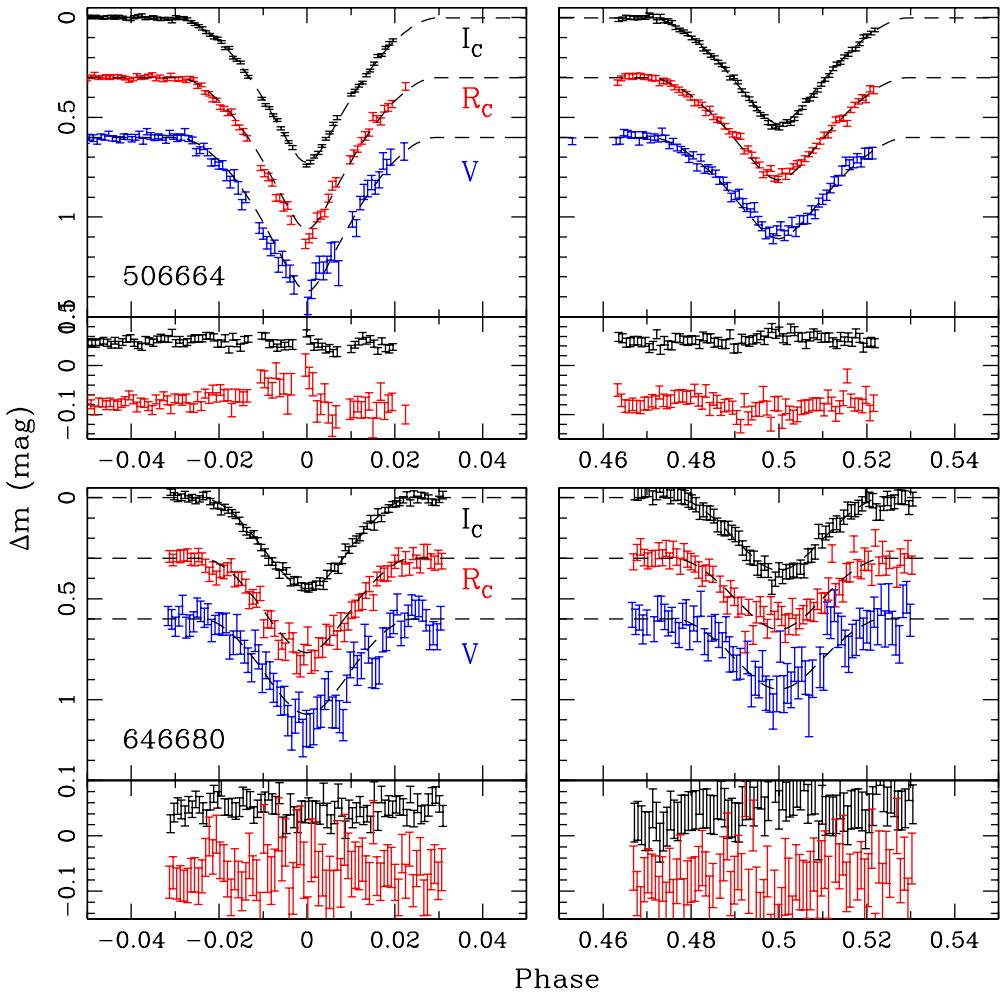

Figure 5. Multicolor eclipse light curves for two more newly discovered M dwarf EB systems: MG1−506664 and MG1−646680. Figure layout and labels are the same as for Figure 4.

(A color version of this figure is available in the online journal.)

All of our new binary systems have orbital periods that are significantly shorter than the canonical limit for tidal circularization (7–10 days; Zahn 1977), so they should have zero eccentricity. This is consistent with the results of our photometric monitoring, which show that all secondary eclipses are displaced by half of the period from the primary eclipse. Given the assumption of circularity, each system's RV curve can be described by a pair of sinusoidal functions with four free parameters: the system period (P), the mean system RV (γ), and the amplitude of each component's RV curve (K_A and K_B). In each case, we hereafter subscript these quantities with "p" to denote the primary star and "s" to denote the secondary star. Since we know the orbital periods from the systems' light curves (Section 5.2), we can further simplify our RV analysis by adopting the previously measured value of P and only fitting for the other three parameters.

For each of our targets, we measured the best-fit values and uncertainties for γ, K_A, and K_B via a χ^2 minimization of the double-sinusoid model:

$$v_p = \gamma - K_A \times \sin(2\pi\theta) \quad (1)$$

$$v_s = \gamma + K_B \times \sin(2\pi\theta). \quad (2)$$

In Figure 8, we show our phased RV observations and the corresponding best-fit models. The models and data show excellent agreement, with a typical dispersion of ∼300 m s^{-1} for all RV measurements where the component spectra were well resolved (i.e., occurring >0.05 phase from an eclipse). There are only a small number of measurements that occurred while the system was near an eclipse, and most are also affected by the Rossiter–McLaughlin effect (Rossiter 1924; McLaughlin 1924). It appears that the uncertainties climb to ∼2.5 km s^{-1} in this regime where the two components' spectra are not clearly resolved. Finally, as we noted above, the total system mass depends on $K_A - K_B$, which in turn can be fit from the velocity difference at each epoch, $(K_A + K_B) = (v_p - v_s) \times \sin(2\pi\theta)$. Since the measurements are treated as a difference of two simultaneous measurements ($v_p - v_s$), any epoch-to-epoch systematic uncertainties would cancel and allow for a more precise mass measurement. However, we found that the resulting masses have similar uncertainties as if we fit for the component masses and combine them. This indicates that the stochastic RV uncertainties are of similar order as the systematic RV uncertainties, and thus that further reduction of the systematic effects is unlikely to improve our measurements.

We summarize our measurements of the observed model parameters (K_A, K_B, and γ) and the corresponding physical system parameters (component masses $M_A \sin^3(i)$ and $M_B \sin^3(i)$, orbital semimajor axis $a \sin(i)$, and component mass ratio q) in Table 8. In all cases, star A is the more massive (primary) star

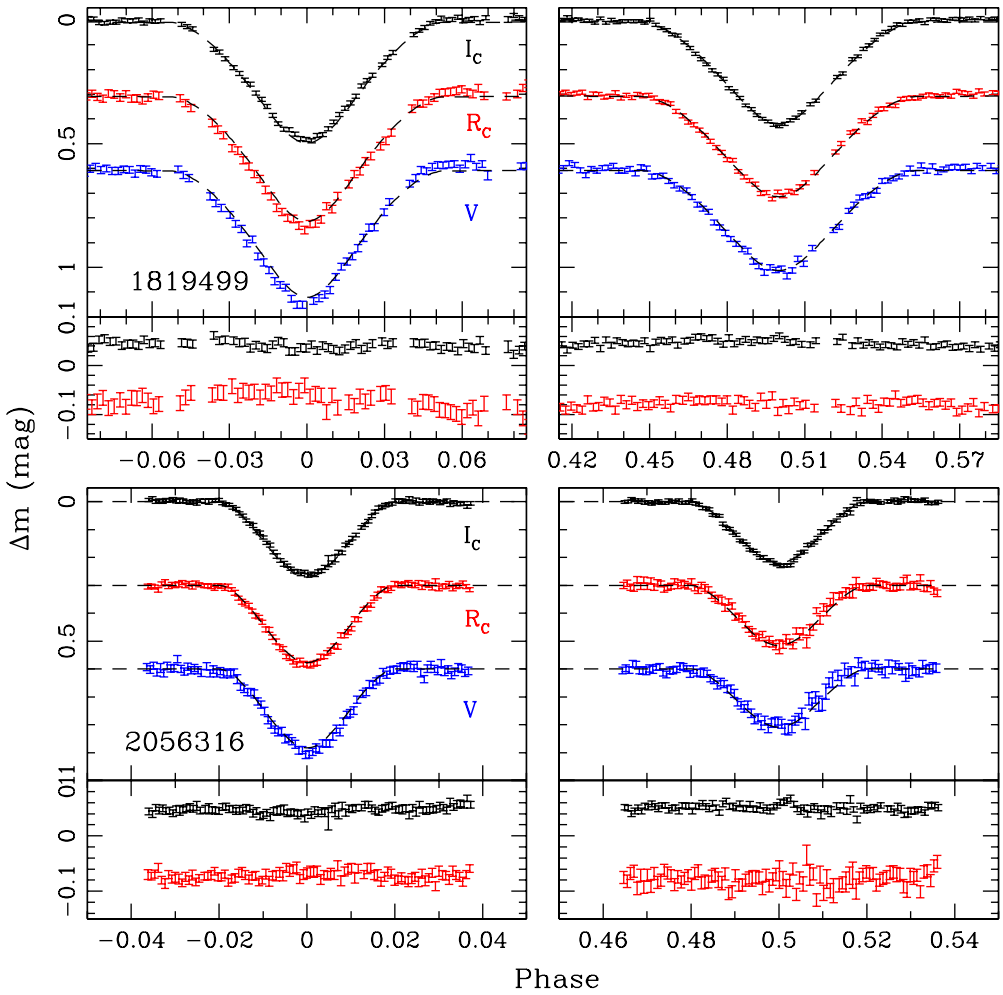

Figure 6. Multicolor eclipse light curves for two more newly discovered M dwarf EB systems: MG1−1819499 and MG1−2056316. Figure layout and labels are the same as for Figure 4.

(A color version of this figure is available in the online journal.)

that is eclipsed (with a deeper amplitude) at phase 0.0 and has a velocity amplitude of K_A.

5.4. Eclipse Fitting

We performed our eclipse-fitting analysis using the 2007 release of the venerable Wilson–Devinney code (WD; Wilson & Devinney 1971), which produces synthetic light curves in a specified set of bandpasses based on a user-defined set of input system parameters. The WD code is packaged with a fitting routine that computes a converging best-fit solution based on differential corrections to an initial estimated solution. However, we found that this fitting routine did not converge well for our data, most likely because we have few observations outside of the eclipses. We instead used the WD code to produce synthetic light curves, then computed the χ^2 goodness-of-fit as compared to our data. While computing our fits, we fixed many of the system parameters (P, q, $a\sin(i)$, and $T_{\rm eff,A}$) to the values computed in the previous sections, and continued to assume that the orbits have been tidally circularized. We adopted a square root limb darkening law as prescribed by van Hamme (1993), including the appropriate temperature-dependent exponents for each component. The only remaining parameters, which we solved for using the WD code, are the orbital inclination i, the component radii r_A and r_B, and the difference in component temperatures ΔT.

We adopted an iterative procedure for finding the best fit. We began by fixing r_A and r_B to a series of initial estimates corresponding to fractional values above and below predictions from theoretical models, with initial values of 95%, 100%, 105%, and 110% of the theoretical radius for that given mass. We then performed a grid search over all values of i and ΔT to find the best fit for those radii. After we had found the best possible solutions for each set of assumed radii, we then relaxed the radius constraints and allowed all four parameters to vary, computing differential corrections in order to converge into the minimum of the χ^2 space. Finally, after we had found a minimum, we performed a grid search of all four parameters around that position in order to confirm that it was a global minimum rather than a local minimum. We accepted a solution only after all four of our initial radius estimates ultimately converged into that minimum, which occurred promptly in all cases and yielded reduced χ^2 values of $\chi^2_\nu = 0.9$–1.9. We computed the uncertainties in our best-fit values of R_A, R_B, i, and ΔT from the shape of the χ^2 surface around that minimum. We summarize the results of this fitting process in Table 8, and, we plot the best-fit models for comparison to each observed light curve in Figures 4–6.

In the majority of cases, we found that the formal uncertainty in the best-fit solution was extremely small. The only exceptions were for MG1−78457 and MG1−646680, where we found ra-

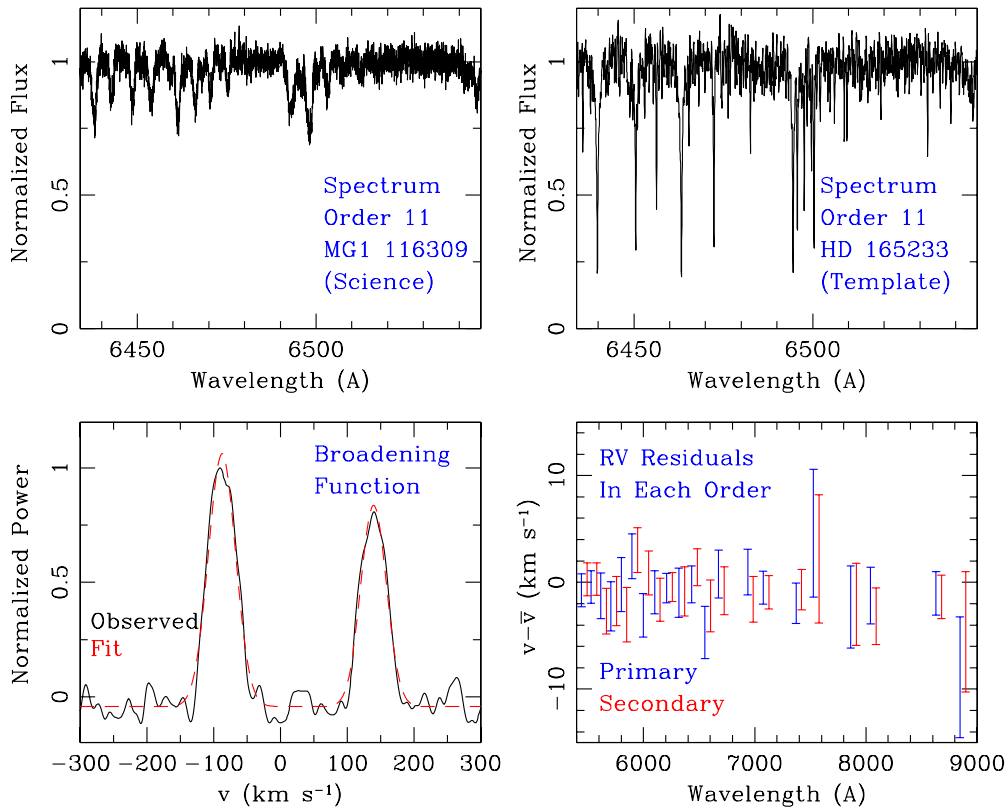

Figure 7. Analysis and results for one HIRES spectrum of MG1−116309. Upper left: one order of the echelle spectrum for MG1−116309, as observed on JD 2454688.1. Upper right: the same echelle order for an RV standard star, HD 165233, which was observed earlier that night. Lower left: the broadening function (black solid line) which, when convolved with the RV standard spectrum, yields the best fit to the science spectrum. The two peaks are well-fit with a pair of Gaussian functions (red dashed line) where the mean of each Gaussian corresponds to the RV difference between that component and the RV standard. Lower right: the residuals as a function of wavelength for the primary (blue) and secondary (red) RV measurements in each order, as measured with respect to the weighted mean of all measurements. Since the residuals often overlap, we offset the secondary point by 0.01 phase.

(A color version of this figure is available in the online journal.)

dius uncertainties of ∼2%. This is a natural consequence of either losing part of an eclipse (as for MG1−78457, due to a flare) and/or using low-quality data (as for MG1−646680, where both eclipses were observed in marginal conditions). In general, the very small uncertainties in our results are not surprising given the volume and precision of our data. Each system had ∼300–600 photometric observations spread between three filters and two eclipse windows, and the uncertainties were $\lesssim$0.01 mag in I_C and $\lesssim$0.05 mag even in V. However, these small stochastic uncertainties suggest that our true uncertainties could be driven by systematic effects rather than stochastic errors. Several different software packages are commonly used to fit light curves (e.g., Wilson & Devinney 1971; Popper & Etzel 1981; Southworth et al. 2004; Prsa & Zwitter 2005), so it seems possible that the choice of algorithm could be significant. However, we used our procedures to re-fit the R_C and I_C light curves reported for GU Boo by López-Morales & Ribas (2005), and given the same spot model, we found the same parameters to within ∼1%. As long as other authors have conducted similar tests, then we expect that this systematic uncertainty will be of similar order. We have also reported all of our photometry and RVs in order to allow future calibration of our results against other algorithms.

Otherwise, the most likely source of systematic uncertainty may be in the likely presence of star spots that can introduce extra variability. Previous observations of low-mass eclipsing systems like GU Boo have found that the inferred radii can change by ∼1%–2% depending on the details of spot modeling (e.g., López-Morales & Ribas 2005 versus Morales et al. 2009); observations of other systems also find spots to be significant at this level (e.g., Irwin et al. 2009; Windmiller et al. 2010). A model for the spot distribution can be inferred from a well-sampled light curve that covers most of an eclipsing system's orbital period; since these stars are tidally locked, then the spots modulate the overall brightness of the system on the same period as the orbital period, and the phase of these modulations sets the longitudinal distribution of spots. However, we observed our systems only around the time of eclipse, so we do not have sufficient information to construct a spot model. We knew before conducting these observations that uncertainties in the spot configuration would likely determine the ultimate accuracy of our observations, but since we had limited resources and many targets to observe, we decided to accept this limitation for the purposes of preliminary characterization. Much of the effect should be removed when we renormalize our eclipse light curves using the out-of-eclipse brightness, but we still must determine the level at which remaining variability can influence our results.

To this end, we have conducted a set of "artificial spot" experiments. For each system in our sample, we have constructed an artificial light curve matching the measured system properties and sampled at the same epochs as our observations. We then introduced various spot configurations into these artificial systems and attempted to refit the light curves with spotless models, thereby measuring the effect on the best-fit system properties. It is still unclear what sets the configuration of spots, so instead of adopting random models, we adopt the spot latitudes,

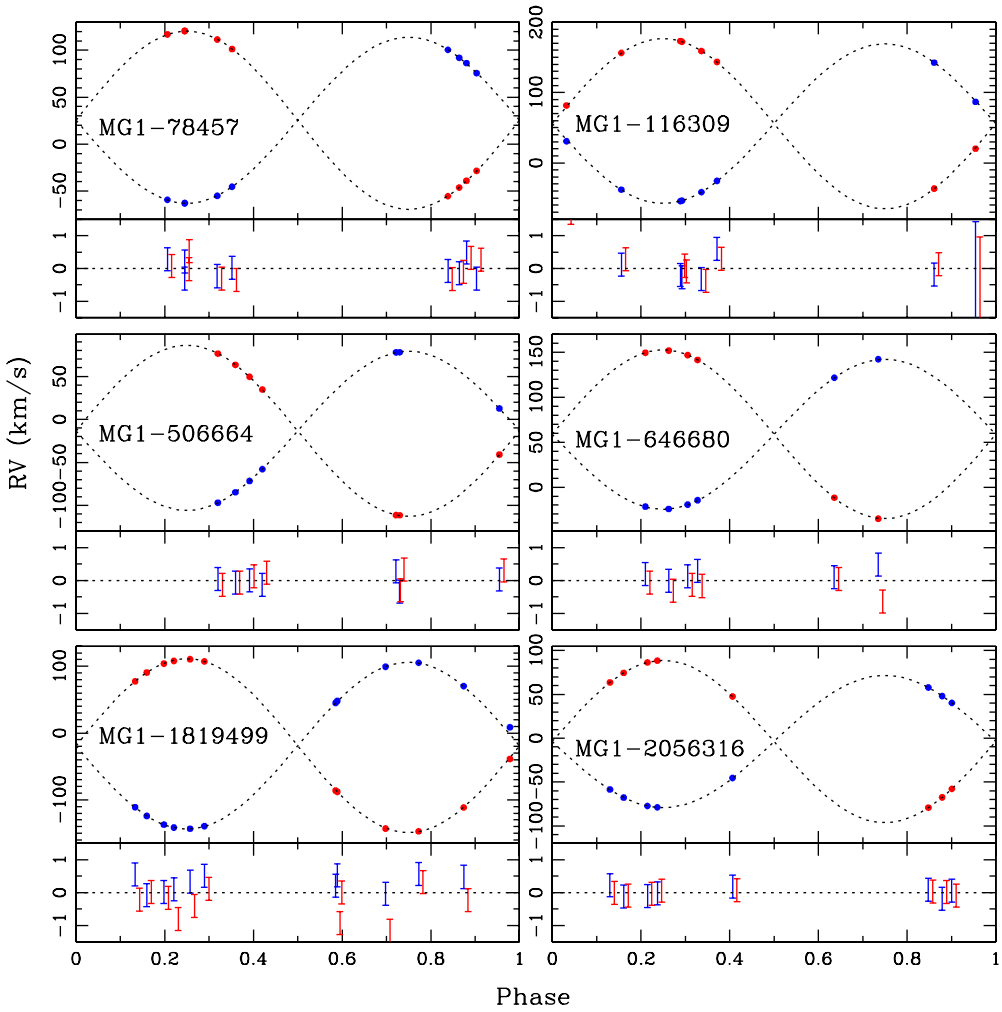

Figure 8. RV curves for our six new M dwarf EBs. For each system, we plot the observed RVs of the primary (blue) and secondary (red), as well as the best-fit sinusoidal RV curves for that system. Underneath each plot, we also show the residuals around the best-fit model.

(A color version of this figure is available in the online journal.)

longitudes, sizes, and temperature ratios inferred for various epochs for CM Dra (M4; Morales et al. 2009) and GU Boo (M0; Windmiller et al. 2010).

We found that uncorrected spots typically led to a dispersion in the inferred system parameters of ∼0.002–0.023 $R_\odot$ for R, ∼0.°05–0.°20 for i, and ∼8–14 K for ΔT. In general, systems are affected more significantly if the eclipses are quick and shallow (as for MG1−1819499). Larger uncertainties are also incurred if there are fewer observations taken before and after the eclipses (as for MG1−116309) since there is a higher uncertainty in renormalizing the constant brightness offset from the spot. In cases like MG1−2056316 or MG1−646680, where both eclipses are bracketed by well-sampled observations, the effect of the spots on the radii is minimal. The effect on ΔT is more significant, and for good reason; if a nontrivial fraction of a star's surface is covered by a spot or plage, then its average temperature is indeed higher or lower than in the unspotted case.

We list the apparent spot-related uncertainties for each system's derived properties in Table 8. However, we suspect that these systematic uncertainties might be overestimated. Our systems have rotational periods that are a factor of ∼2–5 slower than most of the previously studied MDEBs, so they might be less active and show fewer and smaller spots. This is corroborated by our light curves, as most show consistent brightnesses even on very long timescales (e.g., Section 3.1; Figure 2). As we discuss in Section 6, the inferred radii for eight components in four of our systems with similar periods (1.5–1.8 days) and masses (0.35–0.60 $M_\odot$) have model-normalized radii that are typically consistent to within ±2%, which also strongly argues that systematic effects are not significant. However, the components of short-period binary systems do not show such consistency. These systems might be affected by spots, though the similar inconsistency for stars with well-determined spot models (like GU Boo; Morales et al. 2009) suggests that there could be a genuine dispersion in stellar radii.

Finally, we note that light-curve fits generally provide a much stronger constraint on the sum of the radii (which corresponds to the eclipse duration) than on the individual component radii (which only affect the detailed shape of each eclipse). As a result, light-curve fits face a degeneracy between the component radii unless the photometry is very precise. We characterized this requirement by using the WD algorithm to simulate systems with the same radius sum ($R_A + R_B$) and different individual radii, and found that a change of 1% in the component radii corresponded to a difference of ∼2 mmag for each point in the eclipse light curve. Our multicolor eclipse light curves typically contain ∼100–200 $R_C I_C$ points with precisions of ∼10 mmag, so the overall fit should allow us to distinguish radii at this

precision. Our results could be systematically incorrect if our light curves include red noise (e.g., Pont et al. 2006), but we have verified that bright constant stars in our fields are typically precise to ∼3–4 mmag, so this suggests that any systematic uncertainty in the radii should have a magnitude of $\lesssim$2%, and hence be comparable to that from unmodeled spots.

Previous studies have also broken this degeneracy by invoking the observed flux ratio from spectral fitting of the high-resolution spectra used for measuring RV curves (e.g., Stassun et al. 2008; Irwin et al. 2009). If the flux ratio is known at a given wavelength, then the appropriate bolometric corrections can be applied in order to infer the system luminosity ratio; this value can then be combined with the observed temperature ratio in order to infer the ratio of the component radii, and hence the individual radii. However, this technique faces a fundamental systematic limit from our imperfect knowledge of bolometric corrections (which we estimate at ∼5% for early M dwarfs; e.g., Leggett et al. 1996), as well as a stochastic limit from the low precision of flux ratios which are derived from rotationally broadened spectra (which we observe to be ∼5% for our HIRES data). Despite these limits, we tested this technique for our targets by measuring the ratio of the component fluxes around the Ca II infrared triplet, which falls near the blackbody peak and is only very weakly temperature dependent on scales of ∼50–100 K (e.g., Cenarro et al. 2002), and then translating the flux ratio to a luminosity ratio by using interpolations of the broadband bolometric corrections we tabulated in Kraus & Hillenbrand (2007), and finally computing radius ratios and component radii by invoking the temperatures we measured in our light-curve fits. These spectroscopically measured component radii are consistent with the photometrically measured component radii to within ∼3%–4%, which matches the scatter expected from observational and systematic errors in this process. However, our light-curve fits typically yield errors which supercede this level of agreement, so we will not use the spectroscopic constraints on the component radii in our subsequent analysis.

6. THE MASS–RADIUS(–PERIOD?) RELATION FOR LOW-MASS ECLIPSING BINARIES

The past decade has seen a revolution in the calibration of fundamental stellar properties. Binary orbit monitoring has yielded many new dynamical mass measurements (Delfosse et al. 2000; Balega et al. 2005; Martinache et al. 2007; Dupuy et al. 2009), precise parallaxes have led to the measurement of highly precise luminosities (Deacon et al. 2005; Henry et al. 2006; Lépine et al. 2009), and temperature and gravity calibrations (while still systematically uncertain) have been significantly refined (Luhman et al. 2003; Lyo et al. 2008; Cruz et al. 2009). The radii of solar-type stars have been studied in similar detail, but corresponding progress for low-mass stars has not maintained the same pace. These radii are a crucial component in testing stellar models because small changes in opacities and convective efficiencies can significantly change the interior structure, leading to significance changes in the expected radius at a given mass (e.g., Mullan & MacDonald 2001; Chabrier et al. 2007).

The sample of low-mass ($\lesssim$0.7 $M_\odot$) stellar radii has been gradually assembled from many sources over the past ∼5 years. The best radius measurements tend to come from eclipsing double-lined spectroscopic binaries (e.g., Morales et al. 2009; Windmiller et al. 2010), which can be studied in detail since both components are easily observable. Some measurements have fractional uncertainties of $\lesssim$1%, though most systems have not been observed with sufficient resources to yield such precision. Many measurements have also come from single-lined or marginally double-lined systems consisting of a higher-mass F/G dwarf and a low-mass M dwarf. These systems can be more difficult to characterize since they are single-lined spectroscopic binaries, but basing the analysis on the better-understood properties of solar-type stars can allow for sufficient precision (∼2%–5%) to be helpful. Finally, the newest technique to yield new radius measurements is long-baseline optical interferometry (e.g., Berger et al. 2006; Demory et al. 2009; Boyajian et al. 2008), which can yield radius measurements for single stars and not just close binaries, but is typically limited to only a small sample of the closest, brightest stars and faces a systematic limit of ∼5% in the determination of masses (Delfosse et al. 2000).

In Figure 9, we show the updated mass–radius relation for our new observations, as well as for all previous measurements that have fractional uncertainties of <3% and fall in the same mass range (0.35–0.65 $M_\odot$). We also show the theoretical mass–radius relations for old (1 Gyr and 5 Gyr) field stars as predicted by the models of Baraffe et al. (1998). The components in four of our newly discovered systems sit very close to the theoretical mass–radius relation, which seems like an encouraging endorsement for the models. However, one or both components for our other two systems sit significantly above the model sequence, as do most measurements obtained in previous studies; this trend has been well known for several years (e.g., López-Morales 2007). We do not expect a dispersion this large from systematic effects (Section 5.4), so it seems plausible that the variations in observed stellar properties could be genuinely astrophysical in origin, perhaps due to variations in stellar activity and magnetic fields that change the convective efficiency in stellar envelopes (e.g., Mullan & MacDonald 2001; Chabrier et al. 2007).

Close binaries are known to be significantly more active than wide binaries and single stars (e.g., Shkolnik et al. 2010), most likely due to their tidally locked high rotational velocities. Most of the known low-mass EBs show Hα in emission, including all of our newly discovered systems (Table 8), while typical early-M stars show significant Hα emission only within $\lesssim$1 Gyr after formation (West et al. 2008). If this rotation-driven activity is the root cause for MDEBs' inflated radii, then we might expect longer-period systems (with correspondingly lower rotational velocities) to show a smaller effect, and eventually to reach the same mass–radius relation as for single stars. This hypothesis has been difficult to test because the vast majority of known systems have very short periods ($\lesssim$0.5–1.0 days), and the few known long-period systems have not been characterized to high precision. However, our sample includes several systems with periods of 1.5–2.0 days. We therefore can test for a difference in the radii of "short-period" and "long-period" systems, where the sample is divided to yield two equally sized samples. There are no precisely characterized systems with periods of 0.85–1.5 days, so the division could be placed anywhere in this range.

In Figure 10, we plot the model-normalized radius ($R_{\rm obs}/R_{\rm model}$) as a function of the orbital period for all of the known EB systems that have component masses of 0.35–0.80 $M_\odot$ and fractional uncertainties of <3% in their masses and radii. Each measurement has an uncertainty in $R_{\rm obs}/R_{\rm model}$ that encompasses the direct error in $R_{\rm obs}$ as well as the implicit error in $R_{\rm model}$ that comes from the uncertainty in $M_{\rm obs}$; the uncertainties in period are negligible on this scale.

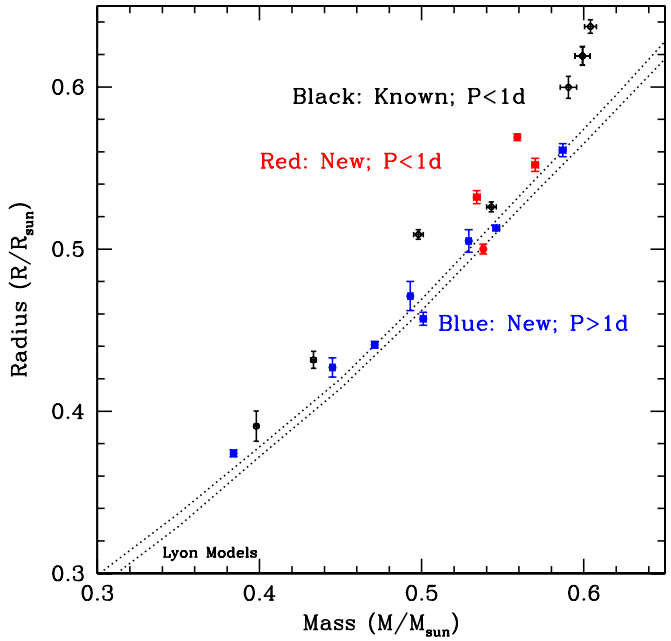

Figure 9. Masses and radii measured for our 12 sample members (filled red: $P < 1$ day; filled blue: $P > 1$ day) and eight components of known M dwarf EBs with parameters measured to $\leqslant$3% precision (open black; Torres & Ribas 2002; Ribas 2003; López-Morales et al. 2006; Windmiller et al. 2010). The dotted lines show the mass–radius relation predicted by the low-mass stellar models of Baraffe et al. (1998) at ages of 1 Gyr (lower) and 5 Gyr (upper). Many low-mass stars appear to sit well above the theoretical mass–radius relation, with some excesses as large as 10%. However, the significant scatter observed between stars (and even between components of the same system) indicates that an additional factor could influence stellar radii.

(A color version of this figure is available in the online journal.)

Short-period systems ($P \lesssim 1$ day) are systematically larger ($+4.8 \pm 1.0$%, with standard deviation of 3.4%) in $R_{\rm obs}/R_{\rm model}$, with some radii up to 10% larger than the models. In contrast, most systems (including all of our new systems) with periods of $\sim$1.5–2.0 days show much better agreement with theoretical predictions ($+1.7\% \pm 0.7\%$, with standard deviation of 2.4%), and only 1/12 is >5% larger than model predictions. The mean radii for the two populations are therefore distinct with a significance of 2.6σ. It is also plausible that the dispersion for long-period systems could result from differences in analysis techniques; our four systems alone have a dispersion of only $\pm$1.8%. In contrast, most of the dispersion for short-period systems can be seen between components of the same system. The components of NSVS0103, GU Boo, and NGC 2204-S892 differ by $6.0\% \pm 1.3\%$, $3.3\% \pm 1.8\%$, and $5.3\% \pm 3.5\%$, respectively.

This trend seems to confirm that close EB systems are indeed inflated in comparison to most low-mass stars, and since they are poor representatives of typical low-mass stars, then any discrepancies with respect to theoretical models should not be taken as an indictment of those models. There are no predictions for the functional form of the radius–period relation, so detailed analysis will require additional theoretical guidance. Current observations do not sample parameter space with enough detail to predict an empirical relation, but the flood of new MDEBs expected from upcoming surveys (e.g., Dupuy et al. 2009) should allow us to address this shortcoming while new theoretical results are in development. In particular, the top priority for these programs should be to characterize systems with even longer periods. On average, the 12 components of long-period systems in our sample agree with stellar evolutionary models to within $\lesssim$2%. However, it seems plausible that the radius–period relation could continue to decline for longer-period systems, such that long-period binaries and single stars are actually smaller than models would predict. Additional high-precision measurements also will allow us to test theoretical models with higher precision. Our results for long-period systems in Figure 10 suggest that the models do still underpredict radii by $1.7\% \pm 0.7\%$.

Alternative explanations must also be considered and ruled out. For example, Morales et al. (2010) suggested that the radius discrepancies might not be a genuine trend, but instead a measurement artifact resulting from nonuniform spot coverage on active stars, and particularly from heavy spotting on the stellar poles. This hypothesis is difficult to distinguish from the convective inefficiency hypothesis since both should result in smaller radii (apparent or real) in longer-period systems. We suggest that one possible test might be to measure radii as a function of binary impact parameters. Grazing-incidence eclipses will occult a higher relative fraction of spotted area than central eclipses will occult, resulting in larger apparent radii. Our current sample is not large enough to see any apparent trend, but future surveys should discover and characterize many more systems. Multi-wavelength observations might also serve to test the spot hypothesis, as the contrast between photospheres and spots is less severe at long wavelengths. Our existing observations do not reveal a significant trend between observation wavelength and measured radius because the uncertainties in our V and R light curves are too large. However, this test should be pursued for bright systems like GU Boo, ideally with larger-aperture telescopes than have been used in the past.

7. SUMMARY

We have discovered and characterized six new M dwarf EB systems, doubling the number of such systems with well-characterized masses and radii ($\sigma \lesssim 3\%$). The components of these systems have masses of 0.38–0.59 $M_{\odot}$ and orbital periods of 0.6–1.7 days. The shorter-period systems in our sample ($P \lesssim 1$ day) tend to follow an elevated mass–radius relation that is consistent with the results seen for previous systems, most of which also have short periods. The components have radii which are up to 10% larger than are predicted by stellar evolutionary models ($\mu = 4.8\% \pm 1.0\%$), and the scatter in this relation is significantly larger than would be expected from the uncertainties. In contrast, longer-period systems have radii that are consistently closer to those the models predict ($\mu = 1.7\% \pm 0.7\%$).

In light of these results, we conclude that the radii of short-period ($\lesssim$1 day) EBs are most likely inflated in comparison to most low-mass stars, and hence they are not good representatives for testing stellar evolutionary models. Since these systems show signs of high chromospheric activity, including Hα emission and significant spot coverage, it seems very plausible that the excess radius is a result of rotation-driven activity in these tidally locked rapid rotators, as was suggested by Chabrier et al. (2007) and is indicated by general models of active stars (Mullan & MacDonald 2001). Longer-period systems seem to be much more consistent in comparison to each other and the models, so they are likely to be better subjects for calibrating the models. However, even though these systems are tidally locked into slower rotational periods, they still rotate faster than their single brethren, plus they still show some signs of heightened activity (including Hα emission with similar line fluxes as for short-period systems). We suggest that this assertion should be tested for systems with even longer periods. Our new systems also do

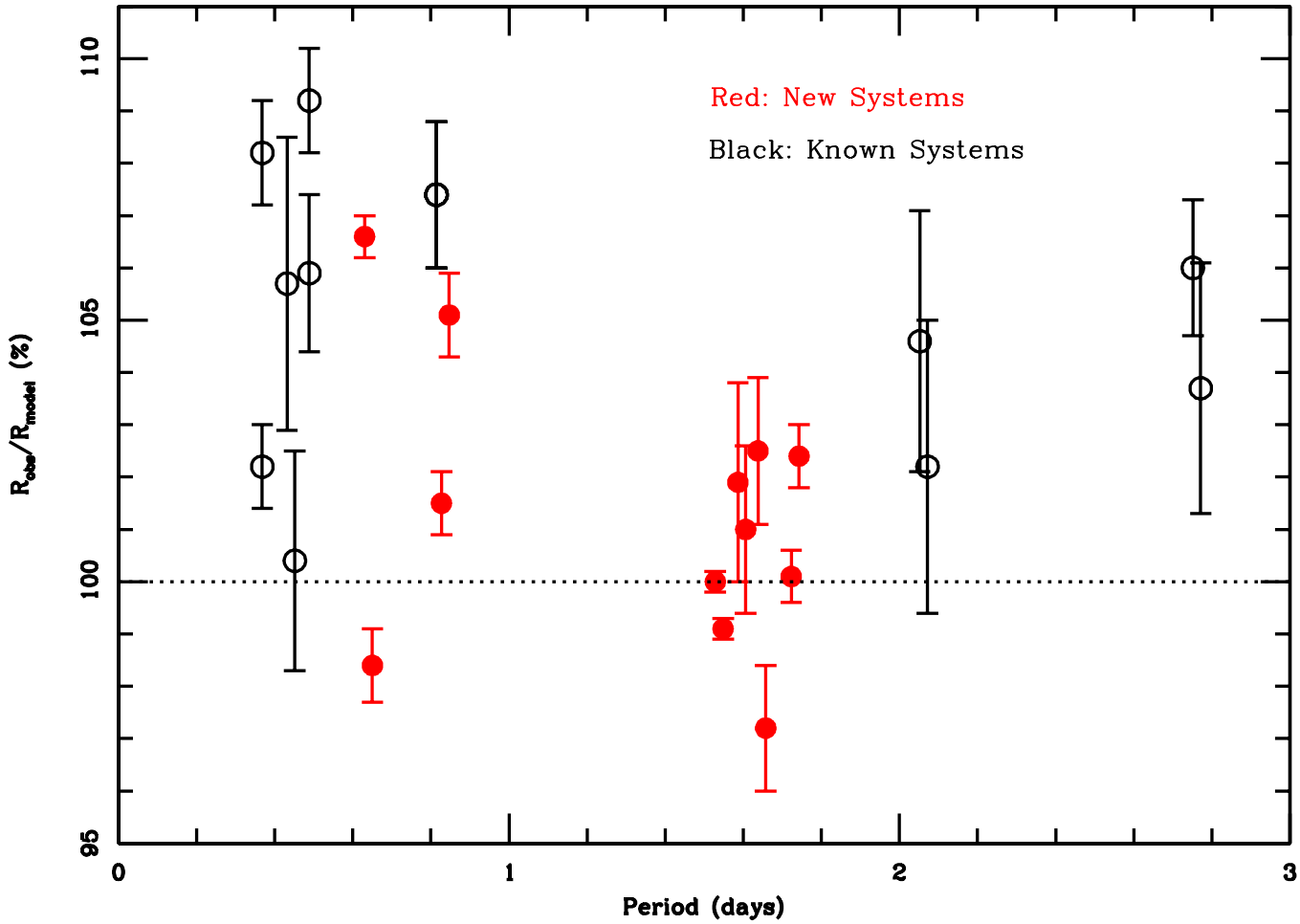

Figure 10. Fractional radius discrepancy (R_{obs}/R_{model}) as a function of orbital period for our newly identified EB systems (filled red) and known systems (open black). In order to isolate a possible period dependence, we use only a restricted range of component masses (0.35–0.80 $M_{\odot}$) and neglect measurements from the literature which are uncertain by >3%, leaving the 12 components of our new systems and 12 components of systems from the literature (Torres & Ribas 2002; Ribas 2003; López-Morales et al. 2006; López-Morales & Shaw 2007; Windmiller et al. 2010; Rozyczka et al. 2009). Short-period systems show a significant spread in radius, such that some components are consistent with the models while others are too large by up to 10%. In contrast, the radii of long-period systems tend to consistently be closer to model predictions. We suggest that short-period systems tend to be inflated because their fast rotation leads to strong magnetic fields that inhibit convection (e.g., Mullan & MacDonald 2001; Chabrier et al. 2007); it is still unclear why two components in the same system can be inflated by different amounts.

(A color version of this figure is available in the online journal.)

not probe the fully convective regime, which could be subject to different physics than for stars with convective envelopes and radiative cores.

Finally, the high yield of our survey (which doubles the available sample of low-mass EBs) suggests that a similar strategy (deep, sparsely sampled observations over a limited area) could be more rewarding than surveys that observe a wider area with shallower limits. As we will report in subsequent publications, the MG1 survey of 300 deg^2 to a limiting magnitude of $R \sim 18$ (Kraus et al. 2007) has uncovered at least 20 new systems with M spectral types, and we have now finished four additional surveys. By covering ∼4% of the sky to a depth that is ∼5 magnitudes deeper, we have achieved a survey volume that is ∼40 times larger than all-sky surveys like ASAS and ROTSE. In the longer term, synoptic all-sky surveys like Pan-STARRS should dwarf even our current efforts (e.g., Dupuy & Liu 2009), though care must be taken not to discover only sources that are too faint for follow-up.

The authors thank C. Slesnick, G. Herczeg, A.M. Cody, M. Ireland, M. Liu, T. Dupuy, J. Johnson, T. Boyajian, M. López-Morales, and K. Stassun for helpful discussions and suggestions, as well as Mansi Kasliwal for her assistance in scheduling the observations with the Palomar 60″ telescope. They also thank the anonymous referee for providing a prompt and helpful review. The analysis in this paper used two existing data analysis pipelines, MAKEE by Tom Barlow and BFall by Slavek Rucinski; the authors gratefully acknowledge their contribution to the field by developing and supporting this software. Some of the data products for this project were provided by a collaboration between the Global Network of Astronomical Telescopes, Inc., and the Moving Object and Transient Event Search System. This work also makes use of data products from 2MASS, which is a joint project of the University of Massachusetts and IPAC/Caltech, funded by NASA and the NSF. A.L.K. was supported by NASA through Hubble Fellowship grant 51257.01 awarded by the Space Telescope Science Institute, which is operated by the Association of Universities for Research in Astronomy, Inc., for NASA, under contract NAS 5-26555. This research was partially supported by a grant to GNAT, Inc., from the American Astronomical Society.

REFERENCES

Akerlof, C., et al. 2003, PASP, 115, 132
Balega, I., Balega, Y., Hofmann, K.-H., Pluzhnik, E., Schertl, D., Shkhogosheva, Z., & Weigelt, G. 2005, A&A, 433, 591
Baraffe, I., Chabrier, G., Allard, F., & Hauschildt, P. 1998, A&A, 337, 403
Bayless, A., & Orosz, J. 2006, ApJ, 651, 1155
Berger, D., et al. 2006, ApJ, 644, 475
Boyajian, T., et al. 2008, ApJ, 683, 424
Cenarro, A., Gorgas, J., Cardiel, N., Vazdekis, A., & Peletier, R. 2002, MNRAS, 329, 863
Cenko, S. B., et al. 2006, PASP, 118, 1396
Chabrier, G., et al. 2007, A&A, 472, 17
Creevy, O., et al. 2005, ApJ, 625, 127
Cruz, K., Kirkpatrick, J. D., & Burgasser, A. 2009, AJ, 137, 3345
Deacon, N., Hambly, N., Henry, T., Subasavage, J., Brown, M., & Jao, W.-C. 2005, AJ, 129, 409
Delfosse, X., Forveille, T., Segransan, D., Beuzit, J.-L., Udry, S., Perrier, C., & Mayor, M. 2000, A&A, 364, 217
Demory, B.-O., et al. 2009, A&A, 505, 205
Dupuy, T., & Liu, M. 2009, ApJ, 704, 1519
Dupuy, T., Liu, M., & Bowler, B. 2009, ApJ, 706, 328
Henry, T., Jao, W.-C., Subasavage, J., Beaulieu, T., Ianna, P., Costa, E., & Méndez, R. 2006, AJ, 132, 2360
Honeycutt, R. 1992, PASP, 104, 435
Irwin, J., et al. 2009, ApJ, 701, 1436
Kraus, A., Craine, E., Giampapa, M., Scharlach, W., & Tucker, R. 2007, AJ, 134, 1488
Kraus, A., & Hillenbrand, L. 2007, AJ, 134, 2340
Lacy, C. 1977, ApJ, 218, 444
Leggett, S., Allard, F., Berriman, G., Dahn, C., & Hauschildt, P. 1996, ApJS, 104, 117
Lépine, S., Thorstensen, J., Shara, M., & Rich, R. 2009, AJ, 137, 4109
Leung, K., & Schneider, D. 1978, AJ, 83, 618
López-Morales, M. 2007, ApJ, 660, 732
López-Morales, M., & Ribas, I. 2005, ApJ, 631, 1120
López-Morales, M., Orosz, J., Shaw, J., Havelka, L., Arevalo, M., McIntyre, T., & Lazaro, C. 2006, arXiv:astro-ph/0610225
López-Morales, M., & Shaw, J. 2007, in ASP Conf. Ser. 362, The Seventh Pacific Rim Conference on Stellar Astrophysics, ed. Y. W. Kang et al. (San Francisco, CA: ASP), 26
Luhman, K., Stauffer, J., Muench, A., Rieke, G., Lada, E., Bouvier, J., & Lada, C. 2003, ApJ, 593, 1093
Lyo, A.-R., Lawson, W., & Bessell, M. 2008, MNRAS, 389, 1461
Maceroni, C., & Montalban, J. 2004, A&A, 426, 577
Martinache, F., Lloyd, J., Ireland, M., Yamada, R., & Tuthill, P. 2007, ApJ, 661, 496
Massey, P., Strobel, K., Barnes, J., & Anderson, E. 1988, ApJ, 328, 315
Mathieu, R., Meibom, S., & Dolan, C. 2004, ApJ, 602, L121
Mazeh, T., & Zucker, S. 1994, Ap&SS, 212, 349
McLaughlin, D. 1924, ApJ, 60, 22
Mighell, K. 2000, in ASP Conf. Ser. 216, Astronomical Data Analysis Software and Systems IX, ed. N. Manset, C. Veillet, & D. Crabtree (San Francisco, CA: ASP), 651
Morales, J., Gallardo, J., Ribas, I., Jordi, C., Baraffe, I., & Chabrier, G. 2010, ApJ, 718, 502
Morales, J., et al. 2009, ApJ, 691, 1400
Mullan, D., & MacDonald, J. 2001, ApJ, 559, 353
Nidever, D., Marcy, G., Butler, R. P., Fischer, D., & Vogt, S. 2002, ApJS, 141, 503
Oke, B., & Gunn, J. 1982, PASP, 94, 586
Plavchan, P., Jura, M., Kirkpatrick, J. D., Cutri, R., & Gallagher, S. 2008, ApJS, 175, 191
Pojmanski, G., et al. 2005, Acta Astron., 55, 275
Pont, F., Zucker, S., & Queloz, D. 2006, MNRAS, 373, 231
Popper, D., & Etzel, P. 1981, AJ, 86, 102
Prsa, A., & Zwitter, T. 2005, ApJ, 628, 426
Reid, I., Hawley, S., & Gizis, J. 1995, AJ, 110, 1838
Ribas, I. 2003, A&A, 398, 239
Rossiter, R. 1924, ApJ, 60, 15
Rozyczka, M., Kaluzny, J., Pietrukowicz, P., Pych, W., Mazur, B., Catelan, M., & Thompson, I. 2009, AcA, 59, 385
Rucinski, S. 1999, in ASP Conf. Ser. 185, Precise Stellar Radial Velocities, ed. J. B. Hearnshaw & C. D. Scarfe (San Francisco, CA: ASP), 82
Shkolnik, E., Hebb, L., Liu, M., Reid, I. N., & Cameron, A. 2010, ApJ, 716, 1522
Skrutskie, M., et al. 2006, AJ, 131, 1163
Slesnick, C., Carpenter, J., & Hillenbrand, L. 2006a, AJ, 131, 3016
Slesnick, C., Carpenter, J., Hillenbrand, L., & Mamajek, E. 2006b, AJ, 132, 2665
Southworth, J., Maxted, P., & Smalley, B. 2004, MNRAS, 351, 1277
Stassun, K., Mathieu, R., Cargile, P., Aarnio, A., Stempels, E., & Geller, A. 2008, Nature, 453, 1079
Stassun, K., Mathieu, R., & Valenti, J. 2006, Nature, 440, 311
Stetson, P. 1987, PASP, 99, 191
Torres, G., & Ribas, I. 2002, ApJ, 567, 1140
Tucker, R. 2007, AJ, 134, 1483
van Hamme, W. 1993, AJ, 106, 2096
Welch, D., & Stetson, P. 1993, AJ, 105, 1813
West, A., et al. 2008, AJ, 135, 785
Wilson, R., & Devinney, E. 1971, ApJ, 166, 605
Windmiller, G., Orosz, J., & Etzel, P. 2010, ApJ, 712, 1003
Woolf, V., & Wallerstein, G. 2006, PASP, 118, 218
Zahn, J.-P. 1977, A&A, 57, 383